



<b>Publication Year</b>	2016
<b>Acceptance in OA</b>	2021-01-08T15:34:06Z
<b>Title</b>	4.5 Years of Multi-wavelength Observations of MRK 421 During the ARGO-YBJ and FERMI Common Operation Time
<b>Authors</b>	Bartoli, B., Bernardini, P., Bi, X. J., Cao, Z., Catalanotti, S., Chen, S. Z., Chen, T. L., Cui, S. W., Dai, B. Z., D'Amone, A., Danzengluobu, De Mitri, I., D'Ettorre Piazzoli, B., Di Girolamo, T., Di Sciascio, G., Feng, C. F., Feng, Zhaoyang, Feng, Zhenyong, Gou, Q. B., Guo, Y. Q., He, H. H., Hu, Haibing, Hu, Hongbo, Iacovacci, M., Iuppa, R., Jia, H. Y., Labaciren, Li, H. J., Liu, C., Liu, J., Liu, M. Y., Lu, H., Ma, L. L., Ma, X. H., Mancarella, G., Mari, S. M., Marsella, G., Mastroianni, S., Montini, P., Ning, C. C., Perrone, L., Pistilli, P., Salvini, P., Santonico, R., Shen, P. R., Sheng, X. D., Shi, F., Surdo, A., Tan, Y. H., VALLANIA, PIERO, VERNETTO, Silvia Teresa, Vigorito, C., Wang, H., Wu, C. Y., Wu, H. R., Xue, L., Yang, Q. Y., Yang, X. C., Yao, Z. G., Yuan, A. F., Zha, M., Zhang, H. M., Zhang, L., Zhang, X. Y., Zhang, Y., Zhao, J., Zhaxiciren, Zhaxisangzhu, Zhou, X. X., Zhu, F. R., Zhu, Q. Q., ARGO-YBJ Collaboration
<b>Publisher's version (DOI)</b>	10.3847/0067-0049/222/1/6
<b>Handle</b>	<a href="http://hdl.handle.net/20.500.12386/29614">http://hdl.handle.net/20.500.12386/29614</a>
<b>Journal</b>	THE ASTROPHYSICAL JOURNAL SUPPLEMENT SERIES
<b>Volume</b>	222



## 4.5 YEARS OF MULTI-WAVELENGTH OBSERVATIONS OF MRK 421 DURING THE ARGO-YBJ AND FERMI COMMON OPERATION TIME

B. BARTOLI<sup>1,2</sup>, P. BERNARDINI<sup>3,4</sup>, X. J. BI<sup>5</sup>, Z. CAO<sup>5</sup>, S. CATALANOTTI<sup>1,2</sup>, S. Z. CHEN<sup>5</sup>, T. L. CHEN<sup>6</sup>, S. W. CUI<sup>7</sup>, B. Z. DAI<sup>8</sup>, A. D'AMONE<sup>3,4</sup>, DANZENGLUOBU<sup>6</sup>, I. DE MITRI<sup>3,4</sup>, B. D'ETTORRE PIAZZOLI<sup>1,2</sup>, T. DI GIROLAMO<sup>1,2</sup>, G. DI SCIASCIO<sup>9</sup>, C. F. FENG<sup>10</sup>, ZHAOYANG FENG<sup>5</sup>, ZHENYONG FENG<sup>11</sup>, Q. B. GOU<sup>5</sup>, Y. Q. GUO<sup>5</sup>, H. H. HE<sup>5</sup>, HAIBING HU<sup>6</sup>, HONGBO HU<sup>5</sup>, M. IACOVACCI<sup>1,2</sup>, R. IUPPA<sup>9,12</sup>, H. Y. JIA<sup>11</sup>, LABACIREN<sup>6</sup>, H. J. LI<sup>6</sup>, C. LIU<sup>5</sup>, J. LIU<sup>8</sup>, M. Y. LIU<sup>6</sup>, H. LU<sup>5</sup>, L. L. MA<sup>5</sup>, X. H. MA<sup>5</sup>, G. MANCARELLA<sup>3,4</sup>, S. M. MARI<sup>13,14</sup>, G. MARSELLA<sup>3,4</sup>, S. MASTROIANNI<sup>2</sup>, P. MONTINI<sup>9</sup>, C. C. NING<sup>6</sup>, L. PERRONE<sup>3,4</sup>, P. PISTILLI<sup>13,14</sup>, P. SALVINI<sup>15</sup>, R. SANTONICO<sup>9,12</sup>, P. R. SHEN<sup>5</sup>, X. D. SHENG<sup>5</sup>, F. SHI<sup>5</sup>, A. SURDO<sup>4</sup>, Y. H. TAN<sup>5</sup>, P. VALLANIA<sup>16,17</sup>, S. VERNETTO<sup>16,17</sup>, C. VIGORITO<sup>17,18</sup>, H. WANG<sup>5</sup>, C. Y. WU<sup>5</sup>, H. R. WU<sup>5</sup>, L. XUE<sup>10</sup>, Q. Y. YANG<sup>8</sup>, X. C. YANG<sup>8</sup>, Z. G. YAO<sup>5</sup>, A. F. YUAN<sup>6</sup>, M. ZHA<sup>5</sup>, H. M. ZHANG<sup>5</sup>, L. ZHANG<sup>8</sup>, X. Y. ZHANG<sup>10</sup>, Y. ZHANG<sup>5</sup>, J. ZHAO<sup>5</sup>, ZHAXICIREN<sup>6</sup>, ZHAXISANGZHU<sup>6</sup>, X. X. ZHOU<sup>11</sup>, F. R. ZHU<sup>11</sup>, AND Q. Q. ZHU<sup>5</sup>

(THE ARGO-YBJ COLLABORATION)

<sup>1</sup> Dipartimento di Fisica dell'Università di Napoli "Federico II," Complesso Universitario di Monte Sant'Angelo, via Cinthia, I-80126 Napoli, Italy

<sup>2</sup> Istituto Nazionale di Fisica Nucleare, Sezione di Napoli, Complesso Universitario di Monte Sant'Angelo, via Cinthia, I-80126 Napoli, Italy

<sup>3</sup> Dipartimento di Matematica e Fisica "Ennio De Giorgi," Università del Salento, via per Arnesano, I-73100 Lecce, Italy

<sup>4</sup> Istituto Nazionale di Fisica Nucleare, Sezione di Lecce, via per Arnesano, I-73100 Lecce, Italy

<sup>5</sup> Key Laboratory of Particle Astrophysics, Institute of High Energy Physics, Chinese Academy of Sciences, P.O. Box 918, 100049 Beijing, China; [chensz@ihep.ac.cn](mailto:chensz@ihep.ac.cn)

<sup>6</sup> Tibet University, 850000 Lhasa, Xizang, China

<sup>7</sup> Hebei Normal University, 050024, Shijiazhuang Hebei, China

<sup>8</sup> Yunnan University, 2 North Cuihu Road, 650091 Kunming, Yunnan, China

<sup>9</sup> Istituto Nazionale di Fisica Nucleare, Sezione di Roma Tor Vergata, via della Ricerca Scientifica 1, I-00133 Roma, Italy

<sup>10</sup> Shandong University, 250100 Jinan, Shandong, China

<sup>11</sup> Southwest Jiaotong University, 610031 Chengdu, Sichuan, China

<sup>12</sup> Dipartimento di Fisica dell'Università di Roma "Tor Vergata," via della Ricerca Scientifica 1, I-00133 Roma, Italy

<sup>13</sup> Dipartimento di Fisica dell'Università "Roma Tre," via della Vasca Navale 84, I-00146 Roma, Italy

<sup>14</sup> Istituto Nazionale di Fisica Nucleare, Sezione di Roma Tre, via della Vasca Navale 84, I-00146 Roma, Italy

<sup>15</sup> Istituto Nazionale di Fisica Nucleare, Sezione di Pavia, via Bassi 6, I-27100 Pavia, Italy

<sup>16</sup> Osservatorio Astrofisico di Torino dell'Istituto Nazionale di Astrofisica, via P. Giuria 1, I-10125 Torino, Italy

<sup>17</sup> Istituto Nazionale di Fisica Nucleare, Sezione di Torino, via P. Giuria 1, I-10125 Torino, Italy

<sup>18</sup> Dipartimento di Fisica dell'Università di Torino, via P. Giuria 1, I-10125 Torino, Italy

Received 2015 March 22; accepted 2015 November 20; published 2016 January 14

### ABSTRACT

We report on the extensive multi-wavelength observations of the blazar Markarian 421 (Mrk 421) covering radio to  $\gamma$ -rays, during the 4.5 year period of ARGO-YBJ and Fermi common operation time, from 2008 August to 2013 February. These long-term observations, extending over an energy range of 18 orders of magnitude, provide a unique chance to study the variable emission of Mrk 421. In particular, due to the ARGO-YBJ and Fermi data, the entire energy range from 100 MeV to 10 TeV is covered without any gap. In the observation period, Mrk 421 showed both low- and high-activity states at all wavebands. The correlations among flux variations in different wavebands were analyzed. The X-ray flux is clearly correlated with the TeV  $\gamma$ -ray flux, while the GeV  $\gamma$ -rays only show a partial correlation with the TeV  $\gamma$ -rays. Radio and UV fluxes seem to be weakly or not correlated with the X-ray and  $\gamma$ -ray fluxes. Seven large flares, including five X-ray flares and two GeV  $\gamma$ -ray flares with variable durations (3–58 days), and one X-ray outburst phase were identified and used to investigate the variation of the spectral energy distribution with respect to a relative quiescent phase. During the outburst phase and the seven flaring episodes, the peak energy in X-rays is observed to increase from sub-keV to a few keV. The TeV  $\gamma$ -ray flux increases up to 0.9–7.2 times the flux of the Crab Nebula. The behavior of GeV  $\gamma$ -rays is found to vary depending on the flare, a feature that leads us to classify flares into three groups according to the GeV flux variation. Finally, the one-zone synchrotron self-Compton model was adopted to describe the emission spectra. Two out of three groups can be satisfactorily described using injected electrons with a power-law spectral index around 2.2, as expected from relativistic diffuse shock acceleration, whereas the remaining group requires a harder injected spectrum. The underlying physical mechanisms responsible for different groups may be related to the acceleration process or to the environment properties.

**Key words:** BL Lacertae objects: individual (Markarian 421) – galaxies: active – gamma-rays: general – radiation mechanisms: non-thermal

**Supporting material:** machine-readable tables

### 1. INTRODUCTION

Active galactic nuclei (AGNs), one of the most luminous sources of electromagnetic radiation in the universe, are

galaxies with a strong and variable non-thermal emission, believed to be the result of the accretion of mass onto a supermassive black hole (with a mass ranging from  $\sim 10^6$  to  $\sim 10^{10} M_{\odot}$ ) lying at the center of the galaxy. In some cases

( $\leq 10\%$ ), AGNs show powerful and highly collimated relativistic jets shooting out in opposite directions, perpendicular to the accretion disk. The jets emanate from the vicinity of the black hole ( $\sim 0.1$  pc) and extend up to  $\sim 1$  Mpc. They are usually associated with several bright superluminal knots, which appear to be related to the episodic ejection of plasmoid blobs (see, for example, the case of the active galaxy M87; Cheung et al. 2007). The origin of the AGN jets is one of the open problems in astrophysics.

AGNs viewed at a small angle to the axis of the jet are called blazars. They usually show flat radio spectra, strong variability, optical polarization, and  $\gamma$ -ray emission. Blazars include BL Lac objects, which have a lower luminosity and lack of strong emission lines in the optical band, and flat-spectrum radio quasars (FSRQ), which show a higher luminosity with strong and broad emission lines. The strongly Doppler-boosted radiation makes blazars the most extreme class of AGNs, where the boosted emission overwhelms all other emission from the source. Therefore, the observation of blazars allows a deep insight into the physical conditions and emission processes of relativistic jets.

Blazars are the dominant extragalactic source class in  $\gamma$ -rays, as revealed by the *Fermi* Large Area Telescope (LAT) survey at GeV energies (Nolan et al. 2012). Moving to very high energies (VHE,  $> 0.1$  TeV), the BL Lac objects dominate the extragalactic sky. Up to now, 60 AGNs have been established as VHE  $\gamma$ -ray emitters, including 52 BL Lac objects.<sup>19</sup> Although the  $\gamma$ -ray emission from blazars has been studied for about two decades, it is still unclear where and how the emission originates. Observations of the misaligned radio galaxy M87 indicate that VHE  $\gamma$ -rays, at least during flaring periods, seem to originate within the jet collimation region, in the immediate vicinity of the black hole (Acciari et al. 2009a; Abramowski et al. 2012). The high-energy particles responsible for the non-thermal emission are generally believed to be accelerated in the relativistic shock front, described by the theory of diffusive acceleration (for a review, see Kirk & Duffy 1999).

The radiation of a blazar is a broadband continuum ranging from radio through X-rays to  $\gamma$ -rays. The spectral energy distributions (SEDs) are characterized by two distinct bumps, which are believed to be dominated by non-thermal emission. The lower energy component, which peaks in the optical through X-ray, is caused by the synchrotron radiation from relativistic electrons (and positrons) within the jet. The origin of the high-energy  $\gamma$ -ray component is still debated. The general view attributes it to inverse Compton scattering of the synchrotron (synchrotron self-Compton, SSC) or external photons (external Compton, EC) by the same population of relativistic electrons (Dermer et al. 1992; Sikora et al. 1994; Ghisellini et al. 1998). However, the hadronic scenario, which attributes the  $\gamma$ -ray emission to proton-initiated cascades and/or to proton-synchrotron emission in a magnetic field-dominated jet (Aharonian 2000), cannot be excluded.

In this panorama, multi-wavelength observations are of fundamental importance. According to the present measurements, X-rays and VHE  $\gamma$ -rays are correlated during the flaring periods (for reviews, see Wagner 2008; Chen 2013). Recently, a long-term continuous monitoring of Mrk 421 performed by the Astrophysical Radiation with Ground-based Observatory at

YangBaJing (ARGO-YBJ) experiment and different satellite-borne X-ray detectors (Bartoli et al. 2011a) showed a good correlation in terms of flux and spectral index. All the observational features indicate that  $\gamma$ -rays and X-rays have a common origin, supporting the leptonic models. The tight correlation is a challenge for models based on hadronic processes. According to a recent collective evidence (Meyer et al. 2012), the SSC mechanism seems to dominate the emission of BL Lac objects, while the EC component becomes important for FSRQ. The lack of strong emission lines in the radiation of BL Lac objects is also taken as evidence for a minor role of ambient photons (e.g., Krawczynski 2004), favoring the SSC model. In this sense, we can assume that BL Lac objects are less affected by the circumbient background radiation and can be considered as ideal targets for the study of the physical processes within the jets. However, even in the framework of the SSC model, the fundamental question of the origin of the flux and spectral variability, observed on timescales from minutes to years, is still open.

Mrk 421 ( $z = 0.031$ ), classified as a BL Lac object, is one of the brightest VHE  $\gamma$ -ray blazars known. It is a very active blazar with major outbursts, composed of many short flares, about once every two years, in both X-rays and  $\gamma$ -rays (Aielli et al. 2010; Bartoli et al. 2011a; Chen 2013). Actually, it is considered an excellent candidate to study the physical processes within the AGN jets. During the last decade, several coordinated multi-wavelength campaigns focusing on Mrk 421 were conducted, both in response to strong outbursts or as part of dedicated observation campaigns. Complex relations between X-rays and VHE  $\gamma$ -rays spectra were observed in many flares (see our previous review in Bartoli et al. 2011a). However, due to the sparse multi-frequency data during long periods of time, no systematic studies on flux variation and SED evolution were achieved, especially in the  $\gamma$ -ray band. In the beginning of 2009, a multi-frequency observational campaign of Mrk 421 was carried out for 4.5 months with an excellent temporal (except at VHE) and energy coverage from radio to VHE  $\gamma$ -rays. During the entire campaign, however, Mrk 421 showed a low activity at all wavebands (Abdo et al. 2011).

To understand the emission variability and the underlying acceleration and radiation mechanisms in jets, continuous multi-wavelength observations, particularly in X-rays and VHE  $\gamma$ -rays, are crucial. A simultaneous SED could provide a snapshot of the emitting population of particles and also constrain the model parameters at a given time (Zhang et al. 2012; Yan et al. 2014). The shape of particle energy distribution could bring information on the underlying acceleration processes (e.g., Cao & Wang 2013; Yan et al. 2013; Chen 2014; Peng et al. 2014). In the VHE band, Cherenkov telescopes cannot regularly monitor AGNs, because of their limited duty cycle and narrow field of view (FOV). Wide-FOV extensive air showers (EAS) arrays, with high-duty cycles, are more suitable for this purpose. A review on EAS arrays and their observations of AGNs can be found in Chen (2013).

ARGO-YBJ is an EAS array with an energy threshold for primary  $\gamma$ -rays of  $\sim 300$  GeV. For five years ARGO-YBJ continuously monitored the blazar Mrk 421, extending at higher energies the multi-wavelength survey carried out by the Owens Valley Radio Observatory (OVRO), the satellite-borne X-ray detectors *Swift*, the *Rossi X-ray Timing Explorer (RXTE)*, the Monitor of All-sky X-ray Image (MAXI), and the GeV

<sup>19</sup> <http://tevcat.uchicago.edu/> (Version: 3.400, as of 2015 March).

$\gamma$ -ray detector *Fermi*-LAT. In particular, due to the ARGO-YBJ and *Fermi*-LAT data, the high-energy component of Mrk 421 SED has been completely covered without any gap from 100 MeV to 10 TeV. In this paper, we report on the 4.5 year multi-wavelength data recorded from 2008 August to 2013 February, a period that includes several large flares of Mrk 421. Such a long-term, multi-wavelength observation is rare and provides a unique opportunity to investigate on the emission variability of Mrk 421 from radio frequencies to TeV  $\gamma$ -rays.

This work is organized as follows: in Section 2 we summarize the data at different wavelengths collected by both satellite-borne and ground-based detectors. In Section 3 the light curves and SEDs observed by the different detectors are presented. In Section 4 the key parameters of the one-zone SSC emission model are obtained by fitting the data, then the astrophysical implications are discussed in Section 5. A summary is given in Section 6. The cosmology parameters used in this paper are:  $H_0 = 70 \text{ km s}^{-1} \text{ pc}^{-1}$ ,  $\Omega_M = 0.3$ , and  $\Omega_\Lambda = 0.7$ . The redshift of Mrk 421 corresponds to a luminosity distance of 135.9 Mpc.

## 2. MULTI-WAVELENGTH OBSERVATIONS AND ANALYSIS

The present section reviews the available data sets. We briefly summarize the energy range in which each detector works and the data processing steps. More details can be found in the cited references.

### 2.1. ARGO-YBJ VHE $\gamma$ -ray Data

ARGO-YBJ is an EAS detector located at an altitude of 4300m a.s.l. (atmospheric depth  $606 \text{ g cm}^{-2}$ ) at the Yangbajing Cosmic Ray Laboratory (30.11 N, 90.53 E) in Tibet, P.R. China. It is mainly devoted to  $\gamma$ -ray astronomy (Bartoli et al. 2012a, 2012b, 2012c, 2013b, 2014, 2015) and cosmic ray physics (Bartoli et al. 2012d, 2012e, 2013c). The detector consists of a carpet ( $\sim 74 \times 78 \text{ m}^2$ ) of resistive plate chambers (RPCs) with  $\sim 93\%$  of active area, surrounded by a partially instrumented area ( $\sim 20\%$ ) up to  $\sim 100 \times 110 \text{ m}^2$ . Each RPC is read out by 10 pads ( $55.6 \text{ cm} \times 61.8 \text{ cm}$ ) representing the spacetime pixels of the detector. Details of the detector layout can be found in Aielli et al. (2006). Due to the full coverage configuration and the location at high altitude, the detector energy threshold is  $\sim 300 \text{ GeV}$ , much lower than any previous EAS array, as Tibet AS $\gamma$  (Amenomori et al. 2005) and Milagro (Abdo et al. 2014).

The ARGO-YBJ experiment, with a  $\sim 2 \text{ sr}$  FOV, is able to monitor the sources in the sky with a zenith angle less than  $50^\circ$ . At the ARGO-YBJ site, Mrk 421 culminates with a zenith angle of  $8^\circ.1$ , and is observable for 8.1 (4.7) hr per day with a zenith angle less than  $50^\circ$  ( $30^\circ$ ).

The detector, in its full configuration, has been in stable data taking since 2007 November to 2013 February, with 4% of dead time and an average duty cycle higher than 86%. The detector performance and the analysis techniques are extensively discussed in Bartoli et al. (2013a). The detector angular resolution depends on the number of triggered pads  $N_{\text{pad}}$ , ranging from  $1^\circ.7$  for  $N_{\text{pad}} > 20$  to  $0^\circ.2$  for  $N_{\text{pad}} > 1000$ . The median primary energy of  $\gamma$ -rays is  $0.36 \text{ TeV}$  for events with  $N_{\text{pad}} > 20$  and  $8.9 \text{ TeV}$  for  $N_{\text{pad}} > 1000$  (Bartoli et al. 2013a). The light curves presented here are obtained selecting the events with  $N_{\text{pad}} > 60$ , corresponding to a photon median

energy of  $\sim 1.1 \text{ TeV}$ . The cosmic ray background around the source direction is estimated using the *direct integral method* (Fleysher et al. 2004). The spectrum is estimated as described in Bartoli et al. (2011a) by comparing the detected and the expected signal (i.e., the number of events) as a function of  $N_{\text{pad}}$ . Five intervals,  $N_{\text{pad}} = 20\text{--}59$ ,  $60\text{--}99$ ,  $100\text{--}199$ ,  $200\text{--}499$ , and  $>500$ , are considered, corresponding to a  $\gamma$ -ray energy range between  $0.3 \text{ TeV}$  and  $10 \text{ TeV}$ . The spectrum is assumed to follow a single power law (PL):  $f(E) = J_0 \cdot E^{-\alpha}$ . The simulated events are sampled in the energy range from  $10 \text{ GeV}$  to  $100 \text{ TeV}$ . The ARGO-YBJ detector response has been evaluated using a custom Montecarlo simulation (see Guo et al. 2010).

### 2.2. Fermi-LAT HE $\gamma$ -ray Data

*Fermi*-LAT (Atwood et al. 2009) is a pair-conversion telescope, with a FOV of over  $2 \text{ sr}$ , operating in the energy range above  $100 \text{ MeV}$ . *Fermi*-LAT began taking science data in 2008 August. The data used in this work have been downloaded through the Fermi science support center.<sup>20</sup> A circular region of  $15^\circ$  radius centered on Mrk 421 was chosen for the event reconstruction. The analysis was performed using the ScienceTool and the corresponding threads, provided by the *Fermi*-LAT collaboration (Version v9r33p0).<sup>21</sup> Events with zenith angles  $< 100^\circ$  were selected from the *Source* class events, which have the highest probability of being photons. The light curve was created through aperture photometry, which allows a model-independent determination of the flux, including both background and source emission. To build the SED of the source, we used the suggested *gtlike* tool, based on a binned maximum likelihood method. The instrument response function is *P7REP\_SOURCE\_V15*, and the Galactic emission was reproduced using the model of *gll\_iem\_v05\_rev1\_fit*. The model for the extragalactic isotropic diffuse emission was *iso\_source05\_rev1\_txt*. All sources within  $20^\circ$  from the Mrk 421 position were taken into account. The spectral parameters are kept free for the sources within  $10^\circ$ , while are fixed to the values given in the second *Fermi*-LAT catalog (Nolan et al. 2012) for other sources.

To describe the source spectrum from  $100 \text{ MeV}$  to  $500 \text{ GeV}$ , we use two different models: the Power Law model and the LogParabolic model (LP). The latter is described by the expression  $f(E) = J_0 \cdot (E/E_0)^{-(a+b \cdot \log(E/E_0))}$ , where  $E_0$  indicates the normalization energy,  $J_0$  the flux at  $E_0$ ,  $b$  the curvature around the SED peak, and  $a$  the spectral index below the SED peak. Following Nolan et al. (2012), these two models are compared by defining the curvature test statistic  $\text{TS}_{\text{curve}} = (\text{TS}_{\text{LP}} - \text{TS}_{\text{PL}})$ . The significance of the curvature can be approximately estimated as  $\sqrt{\text{TS}_{\text{curve}}}$ .

### 2.3. Swift-BAT Hard X-Ray Data

The *Swift* Burst Alert Telescope (BAT; Gehrels et al. 2004) is a coded aperture mask imaging telescope ( $1.4 \text{ sr}$  FOV) operating since 2005 February. It orbits the Earth every  $1.5 \text{ hr}$  and monitors the entire sky at hard X-rays once per day. The daily flux from Mrk 421 at energy  $15\text{--}50 \text{ keV}$  is provided by *Swift*-BAT<sup>22</sup> (Krimm et al. 2013) and is used here to build the

<sup>20</sup> <http://fermi.gsfc.nasa.gov/ssc/>

<sup>21</sup> <http://fermi.gsfc.nasa.gov/ssc/>

<sup>22</sup> Transient monitor results provided by the *Swift*-BAT team: <http://heasarc.gsfc.nasa.gov/docs/swift/results/transients/weak/>.

light curve. To obtain the SED, we downloaded all the available data of Mrk 421 through the HEASARC data archive.<sup>23</sup> The data analysis includes the recipes presented in Ajello et al. (2008) and Tueller et al. (2010). The spectrum was obtained as a weighted average of the source spectra using a six-channel binning in the 14–195 keV energy range, i.e., 14–22, 22–30, 30–47, 47–71, 71–121, and 121–195 KeV. A power-law function was used to fit the measured spectrum.

#### 2.4. MAXI-GSC X-Ray Data

The MAXI Gas Slit Camera (GSC; Matsuoka et al. 2009) detector, made of 12 one-dimensional position sensitive proportional counters, operating in the 2–20 keV range, began taking data in 2009 August. The experiment achieves 97% of sky coverage per day. The light curves for specific sources are publicly available<sup>24</sup> in three energy bands: 2–4, 4–10, and 10–20 keV. These data were used in this work to build the X-ray spectrum of Mrk 421, comparing the measured counting rate in each band with the one of the Crab Nebula, used as standard candle, as proposed by the *Swift*-BAT collaboration (Tueller et al. 2010).

#### 2.5. RXTE-ASM Soft X-Ray Data

The *RXTE* All Sky Monitor (ASM; Levine et al. 1996) consists of three proportional counters, each one with a FOV of  $6^\circ \times 90^\circ$ . It covers about 80% of the sky during one full revolution in about 1.5 hr. The *RXTE*-ASM data in the (2–12) keV range are publicly available.<sup>25</sup> The light curves are given in three energy bands: 1.5–3, 3–5, and 5–12 keV, which were used here to build the X-ray spectrum. For Mrk 421, the daily flux is provided from 1995 up to the middle of 2010.

#### 2.6. Swift-XRT Soft X-Ray Data

The *Swift* X-ray Telescope (XRT; Burrows et al. 2005) is a focusing X-ray telescope with an energy range from 0.2 to 10 keV. The light curves at 0.3–10 keV for Mrk 421 (available here<sup>26</sup>) were directly used in this work. To obtain the SED, all the *Swift*-XRT Windowed Timing (WT) Observations, available at HEASARC<sup>27</sup>, were downloaded. The *Swift*-XRT data set are calibrated using the calibration files available in the Swift database (CALDB<sup>28</sup>) and processed with the XRTDAS software package (distributed by HEASARC within the HEASoft package (v.6.16)<sup>29</sup>) using the *xrtpipeline* task. Events for the spectral analysis were selected within a circle of 30 pixel (71") radius centered on the source position. The background was extracted from an annular region with a 40 pixel inner radius and 80 pixel outer radius, also centered on the source position. The count rate is less than 100 Hz for all the observations considered in this work, so the WT mode data should not be affected by pile-up effects. The average spectrum

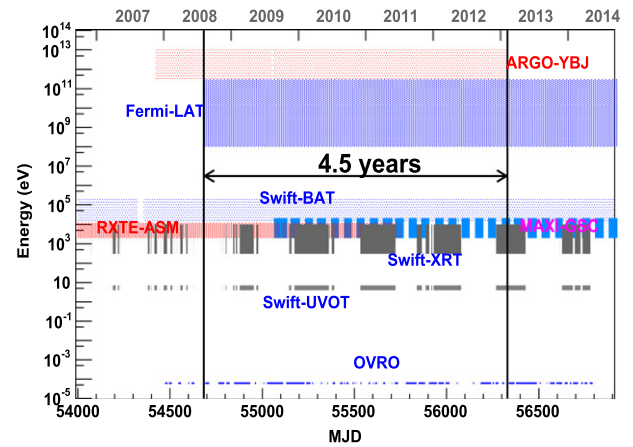


**Figure 1.** Time and energy coverage of different detectors in 4.5 years of Mrk 421 observation.

in the 0.3–10 keV energy band was fitted using the XSPEC package<sup>30</sup> (v.12.8.2), assuming an LP model (fixing  $E_0 = 1$  keV), with an absorption hydrogen-equivalent column density set to the Galactic value in the direction of the source, namely  $1.92 \times 10^{20} \text{ cm}^{-2}$  (Kalberla et al. 2005). For such a spectrum model, the energy of the SED peak is estimated as  $E_{\text{peak}} = 10^{(2-a)/2b}$ . In addition, a small energy offset ( $\sim 40$  eV) was applied to the observed energy spectrum, according to Abdo et al. (2011).

#### 2.7. Swift-UVOT Ultraviolet Data

The *Swift* Ultraviolet/Optical Telescope (UVOT; Roming et al. 2005) is the ultraviolet and optical telescope on board the satellite. All the *Swift*-UVOT observations of Mrk 421, at the three ultraviolet bands (UVW1, UVM2, and UVW2) available at the HEASARC data archive, were included in our analysis. The level 2 UVOT images from the archive, produced by a custom UVOT pipeline with data screening and coordinate transformation, were directly used in this work. The photometry was computed using a 8" source region centered on the Mrk 421 position, performing the calibrations presented in Poole et al. (2008), which also convert UVOT magnitudes to flux units. The latest UVOT calibration files released on 2013 January 18 were used here. The background was extracted from an annular region (with radius of  $20'' - 50''$ ) centered on the source position. The flux has been corrected for the Galactic extinction using the Cardelli et al. (1989) parameterization, with  $E_{B-V} = 0.013$  mag (Schlafly & Finkbeiner 2011).

#### 2.8. OVRO Radio Data

The OVRO (Richards et al. 2011) is a 40 m radio telescope working at 15.0 GHz with 3 GHz bandwidth. Mrk 421 was observed by OVRO as part of the blazar monitoring program, which observed a sample of over 1800 AGNs twice per week. Mrk 421 has been included since the end of 2007. The light curve for Mrk 421 is publicly available<sup>31</sup> and is directly used in this work. The systematic error is estimated to be about 5% of the flux density, which is not included in the error bars.

<sup>23</sup> <http://heasarc.nasa.gov/docs/archive.html>

<sup>24</sup> The MAXI data are provided by RIKEN, JAXA, and the MAXI team: <http://maxi.riken.jp/top/>

<sup>25</sup> Quick-look results provided by the *RXTE*-ASM team: [http://xte.mit.edu/ASM\\_lc.html](http://xte.mit.edu/ASM_lc.html).

<sup>26</sup> <http://www.swift.psu.edu/monitoring/>

<sup>27</sup> <http://heasarc.nasa.gov/docs/archive.html>

<sup>28</sup> [http://heasarc.gsfc.nasa.gov/docs/heasarc/caldb/caldb\\_supported\\_missions.html](http://heasarc.gsfc.nasa.gov/docs/heasarc/caldb/caldb_supported_missions.html)

<sup>29</sup> <http://heasarc.nasa.gov/lheasoft/>

<sup>30</sup> <http://heasarc.gsfc.nasa.gov/xanadu/xspec/>

<sup>31</sup> <http://www.astro.caltech.edu/ovroblazars/>

### 3. RESULTS

Figure 1 summarizes the temporal and energy coverage of the different instruments considered in this analysis. To monitor efficiently the HE and VHE components of Mrk 421 spectrum, we limit the observation time to the  $\sim 4.5$  years in which the data of *Fermi*-LAT ( $100 \text{ MeV} < E < 500 \text{ GeV}$ ) and ARGO-YBJ ( $E > 300 \text{ GeV}$ ) overlap, i.e., since 2008 August 5 (start time of the *Fermi*-LAT science data acquisition) to 2013 February 7 (end time of the ARGO-YBJ data taking).

In the following, we first determine the light curves of Mrk 421 in the energy ranges explored by the different detectors. Then, by inspecting the light curves, we define the flaring and steady phases of the source. Finally, we analyze the general features of the corresponding SEDs.

#### 3.1. Light Curves

Figure 2 shows the light curves of Mrk 421, as obtained by the data of the previously described experiments, covering the entire energy range from the radio to the TeV band. The time integration is chosen taking into account the sensitivity of the instruments. For ARGO-YBJ each point corresponds to 1 month (30 days) of data, while for *Fermi*-LAT, *Swift*-BAT, *RXTE*-ASM, and *MAXI*-GSC the data are averaged over 1 week. For *Swift*-XRT and *Swift*-UVOT, each point is the result of each dwell, which last about hundreds of seconds. Note that since the *Swift*-UVOT light curves in the three photometric bands (UVW1, UVM2, and UVW2) show similar behaviors, only the light curve of UVW1 is considered here. For OVRO, each point is the result of each observation. The data presented in Figure 2 are also listed in Table 1.

According to the long-term light curves presented in Figure 2, Mrk 421 showed both low- and high-activity phases at all wavebands during the 4.5 years considered in this work. To quantify the variability amplitudes in each energy band, the normalized variability amplitude ( $F_{\text{var}}$ ), defined according to Edelson et al. (1996), was computed as

$$F_{\text{var}} = \frac{\sqrt{\sigma_{\text{tot}}^2 - \sigma_{\text{err}}^2}}{\bar{F}}, \quad (1)$$

where  $\sigma_{\text{tot}}$  is the standard deviation of the flux,  $\sigma_{\text{err}}$  is the mean error of the flux points, and  $\bar{F}$  is the mean flux. To facilitate the comparison of  $F_{\text{var}}$  for different bands, we rebinned all light curves shown in Figure 2 with the same bin size, i.e., seven days per bin. The ARGO-YBJ data with seven-day bin sizes are presented in Table 1. The  $F_{\text{var}}$  as a function of band energy is shown in Figure 3. The variability amplitude increases from 21% in radio to 137% in hard X-rays. The amplitude is 39% for GeV  $\gamma$ -rays, and it increases to 84% at TeV energies. It should be noted that the light curve of GeV  $\gamma$ -rays is obtained through the aperture photometry method, which includes a contribution from the background emission at an 18% level according to our estimation. Since the background only affects the average flux and not the variability amplitude, the effective amplitude of GeV  $\gamma$ -ray variability is 47%.

According to Figure 2, only the light curves of *Swift*-BAT, *Fermi*-LAT, and ARGO-YBJ continuously sampled the entire 4.5 year period considered here. Several large X-ray and GeV  $\gamma$ -ray flares are visible from the light curves of *Swift*-BAT and *Fermi*-LAT. The flux variability in the *Swift*-BAT

and *Fermi*-LAT energy bands does not seem to be correlated during flares. The variability of VHE  $\gamma$ -ray flux is roughly correlated both with X-ray and GeV flares. The variability of radio and UV flux does not seem to be correlated with that of X-rays and  $\gamma$ -rays. To be more rigorous, the discrete correlation function (DCF; Edelson & Krolik 1988) is used to quantify the degree of correlation between the light curve of *Swift*-BAT (*Fermi*-LAT and *Swift*-UVOT) with the others. To ensure the data is uniform, the cross-correlation analysis was performed, using weekly binned light curves. No significant time lag (within  $[-200, 200]$  days) was measured in this analysis except between *Fermi*-LAT and ORVO, where it was found that the GeV  $\gamma$ -rays lead the radio by 42 days, with a correlation coefficient  $r = 0.83 \pm 0.27$ . This result is consistent with Hovatta et al. (2015), who also measured a  $40 \pm 9$  days time lag using 4 years of ORVO and *Fermi*-LAT data. Beside this, a possible time lag is measured between the *Swift*-UVOT and ORVO data. The UV flux seems to lead the radio by 21 days with a correlation coefficient  $r = 0.79 \pm 0.17$ , which, however, is comparable to the coefficient  $r = 0.62 \pm 0.14$  obtained for a time lag equal to zero. The correlation coefficients for a time lag of zero are listed in Table 2, for all the data sets. According to our analysis, the *Swift*-BAT hard X-ray flux is weakly anti-correlated with the radio and UV flux, while it is significantly correlated with the soft X-ray flux, not correlated with GeV  $\gamma$ -rays, and clearly correlated with VHE  $\gamma$ -rays. The *Fermi*-LAT GeV  $\gamma$ -ray flux is weakly correlated with radio, UV, and soft X-rays, and moderately correlated with VHE  $\gamma$ -rays. The UV flux appears to be moderately correlated with radio, weakly anti-correlated with X-rays, and clearly anti-correlated with VHE  $\gamma$ -rays. It should be noted, however, that the observation time of *Swift*-UVOT has several long gaps, which would affect the cross-correlation analysis. In particular, the anti-correlation with VHE  $\gamma$ -rays needs to be checked by future observations.

#### 3.2. Source State Definition

In this paper, we will focus on the large X-ray and GeV  $\gamma$ -ray flares, with the aim to investigate the spectral variation at different wavebands, compared to the low-activity states. We will define different states of activity for Mrk 421 mainly basing on the light curves of *Fermi*-LAT and *Swift*-BAT, partially taking into account the curves of *RXTE*-ASM and *MAXI*-GSC. For X-ray flares, we will only select the flares which show a large increase both in hard and soft X-rays.

From 2008 August (MJD = 54683) to 2009 June (MJD = 55000), Mrk 421 shows low activity at all wavebands. We mark this period as a Steady 1 (S1) phase. It should be noted that, during this period, a 4.5 month long multi-frequency campaign was organized (Abdo et al. 2011). Afterwards, according to the X-ray light curves of *Swift*-BAT, *RXTE*-ASM, and *MAXI*-GSC, the source entered a long-lasting outburst phase starting in 2009 June and ending in 2010 June (MJD = 55350), which we denoted as Outburst (OB). The X-ray flux is higher than in the S1 period and also varies with time. During this active phase, three large flares, named Flare 1, Flare 2, and Flare 3 (F1, F2, and F3) are clearly detected both by *Swift*-BAT and *RXTE*-ASM. During F1, the flux starts to increase on 2009 November 9 (MJD = 55144), reaches the maximum on November 12, then decreases to a quasi-steady state on November 14. The average flux is about 3 and 14 times higher than in the S1 phase, in the 2–12 keV and 15–50 keV ranges, respectively. The F2 (from 2010 February 15

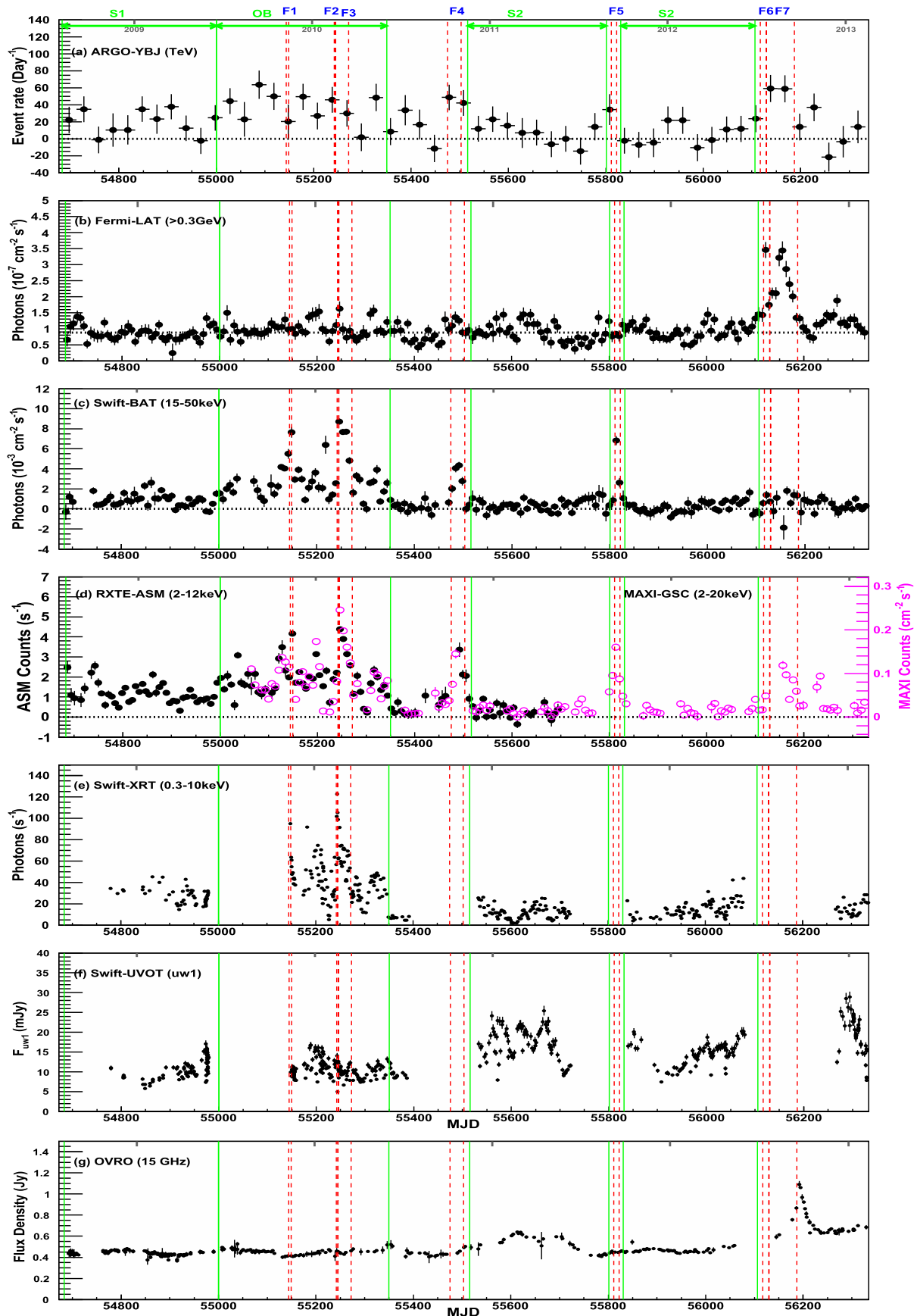


**Figure 2.** Mrk 421 light curves in different energy bands, from 2008 August 5 to 2013 February 7. Each bin of the ARGO-YBJ data contains the event rate averaged over 30 days. Each bin of the *Fermi*-LAT, *Swift*-BAT, *RXTE*-ASM, and *MAXI*-GSC data contains the event rate averaged over seven days. The horizontal dotted line in panel (b) indicates the average flux before F6 and the horizontal dotted lines in the other panels indicate the zero flux.

**Table 1**  
Light Curves Shown in Figure 2

MJD	$\Delta T$ (Day)	Flux <sup>a</sup>	$\Delta$ Flux <sup>a</sup>	Detector
54698.00	15.00	2.231e+01	1.560e+01	ARGO-YBJ
54728.00	15.00	3.486e+01	1.527e+01	ARGO-YBJ
54758.00	15.00	-1.327e+00	1.570e+01	ARGO-YBJ
54788.00	15.00	1.026e+01	1.973e+01	ARGO-YBJ
54818.00	15.00	1.047e+01	1.737e+01	ARGO-YBJ
54848.00	15.00	3.495e+01	1.492e+01	ARGO-YBJ
54878.00	15.00	2.322e+01	1.723e+01	ARGO-YBJ
54908.00	15.00	3.786e+01	1.477e+01	ARGO-YBJ
54938.00	15.00	1.242e+01	1.493e+01	ARGO-YBJ
54968.00	15.00	-2.462e+00	1.544e+01	ARGO-YBJ
54998.00	15.00	2.471e+01	1.505e+01	ARGO-YBJ
55028.00	15.00	4.428e+01	1.520e+01	ARGO-YBJ
55058.00	15.00	2.294e+01	2.037e+01	ARGO-YBJ
55088.00	15.00	6.377e+01	1.677e+01	ARGO-YBJ
55118.00	15.00	4.981e+01	1.594e+01	ARGO-YBJ
55148.00	15.00	2.032e+01	2.004e+01	ARGO-YBJ
55178.00	15.00	4.956e+01	1.539e+01	ARGO-YBJ
55208.00	15.00	2.683e+01	1.561e+01	ARGO-YBJ
55238.00	15.00	4.596e+01	1.528e+01	ARGO-YBJ
55268.00	15.00	2.997e+01	1.557e+01	ARGO-YBJ

**Note.**

<sup>a</sup> The flux units are events day<sup>-1</sup> for ARGO-YBJ, photons cm<sup>-2</sup> s<sup>-1</sup> for *Fermi*-LAT, *Swift*-BAT, and *MAXI*-GSC, photons s<sup>-1</sup> for *RXTE*-ASM and *Swift*-XRT, mJy for *Swift*-UVOT, and Jy for OVRO.

(This table is available in its entirety in machine-readable form.)

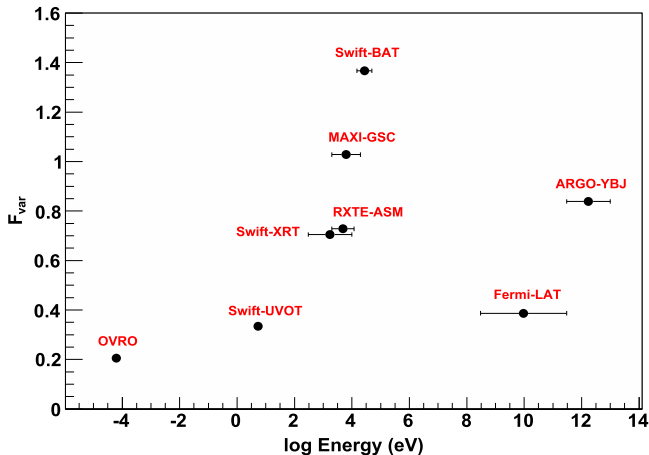


**Figure 3.** Normalized variability amplitude  $F_{\text{var}}$  for different energy bands.

(MJD = 55242) to 17) and F3 (from 2010 February 18 to March 16 (MJD = 55271)) states were reported by *MAXI* at 2–10 keV (Isobe et al. 2010). A zoomed view of the light curves during both flares is shown in Figure 4, with a three-day binning for ARGO-YBJ and one-day binning for the other experiments. F2 is a very fast flare reaching the peak flux in one day and then also decaying in one day. This flare is associated with the huge VHE  $\gamma$ -ray flare with a flux around 10 times the Crab Nebula flux ( $I_{\text{crab}}$ ) detected by VERITAS on February 17 (MJD = 55244; Ong 2010). The  $\gamma$ -ray flux enhancement is also evident in the *Fermi*-LAT and ARGO-YBJ data. F3 follows flare 2. Note that for the OB state, the embedded durations of flares F1, F2, and F3 are excluded.

After 2010 May, Mrk 421 entered a low steady phase that ended on October 6 (MJD = 55475), when the flux of both

**Table 2**  
Correlation Coefficient

	$r_{\text{UVOT}}^a$	$r_{\text{BAT}}^b$	$r_{\text{LAT}}^c$
ORVO	$0.62 \pm 0.14^d$	$-0.26 \pm 0.06$	$0.38 \pm 0.11^e$
<i>Swift</i> -UVOT	...	$-0.35 \pm 0.08$	$0.33 \pm 0.11$
<i>Swift</i> -XRT	$-0.39 \pm 0.08$	$0.85 \pm 0.21$	$0.27 \pm 0.15$
<i>RXTE</i> -ASM	$-0.47 \pm 0.10$	$0.87 \pm 0.17$	$0.38 \pm 0.14$
<i>MAXI</i> -GSC	$-0.34 \pm 0.12$	$0.89 \pm 0.22$	$0.30 \pm 0.10$
<i>Swift</i> -BAT	$-0.35 \pm 0.08$	...	$-0.01 \pm 0.08$
<i>Fermi</i> -LAT	$0.33 \pm 0.11$	$-0.01 \pm 0.08$	...
ARGO-YBJ	$-0.90 \pm 0.33$	$0.76 \pm 0.25$	$0.61 \pm 0.22$

**Notes.**

<sup>a</sup> Cross-correlation coefficient with *Swift*-UVOT.

<sup>b</sup> Cross-correlation coefficient with *Swift*-BAT.

<sup>c</sup> Cross-correlation coefficient with *Fermi*-LAT.

<sup>d</sup> The coefficient at lag = 21 day is  $r = 0.79 \pm 0.17$ .

<sup>e</sup> The coefficient at lag = 42 day is  $r = 0.83 \pm 0.27$ .

hard and soft X-rays started gradually to increase for two weeks. The whole period lasted about one month and is marked as Flare 4 (F4). Then Mrk 421 came to a long and steady phase (S2), both in X-rays and  $\gamma$ -rays, which lasted about 1.6 years, from 2010 November (MJD = 55516) to 2012 June (MJD = 56106). This is the longest steady phase during the monitored period, and therefore it has been selected as a baseline reference to all the other states. The embedded strong flare, denoted as Flare 5 (F5), occurred in September 2011 (MJD = 55811) and lasted  $\sim 7$  days, has been excluded from S2.

In the entire year 2012, the flux in hard X-rays was almost stable, while the GeV  $\gamma$ -ray flux measured by *Fermi*-LAT entered into a high-flux level from 2012 July 9 (MJD = 56117) to September 17 (MJD = 56187). This is the first long-term GeV  $\gamma$ -ray flare from Mrk 421 ever detected, reported by both *Fermi*-LAT (Ammando & Orienti 2012) and ARGO-YBJ (Bartoli et al. 2012f). According to the GeV  $\gamma$ -ray light curve, two peaks are selected, marked as Flare 6 (F6, from 2012 July 9 to 21 (MJD = 56129)) and Flare 7 (F7, from 2012 July 22 to September 16), during which the VHE  $\gamma$ -ray flux detected by ARGO-YBJ also seems to be enhanced. Some hints of enhancement were partly observed by *MAXI*-GSC in the soft X-ray energy range.

The light curves during F1, F4, F5, F6, and F7 are shown in Figure 5, where the flux measured by ARGO-YBJ is averaged over the different flare durations, and a three-day binning is used for the other experiments. The duration of all the selected states are summarized in Table 3. Note that *Swift*-XRT data are only available for the F1, F2, F3, S1, S2, and OB states.

### 3.3. Spectral Energy Distribution

In this section, we report the multi-wavelength SEDs observed by the running experiments in the outlined states.

To model the spectral energy distribution  $f(E)$ , we assume a simple power-law spectrum for *Swift*-BAT, *RXTE*-ASM, *MAXI*-GSC, *Fermi*-LAT, and ARGO-YBJ, while for *Swift*-XRT we assume a logparabolic function. In the following,  $F$  represents the integral flux over the detector energy range,  $\alpha$  the spectral index of the power-law function, while  $a$  and  $b$  the parameters of the logparabolic model (see Section 2 for details). During S2, the *Swift*-BAT data are not significant enough to fit both the flux and the spectral index. For such a

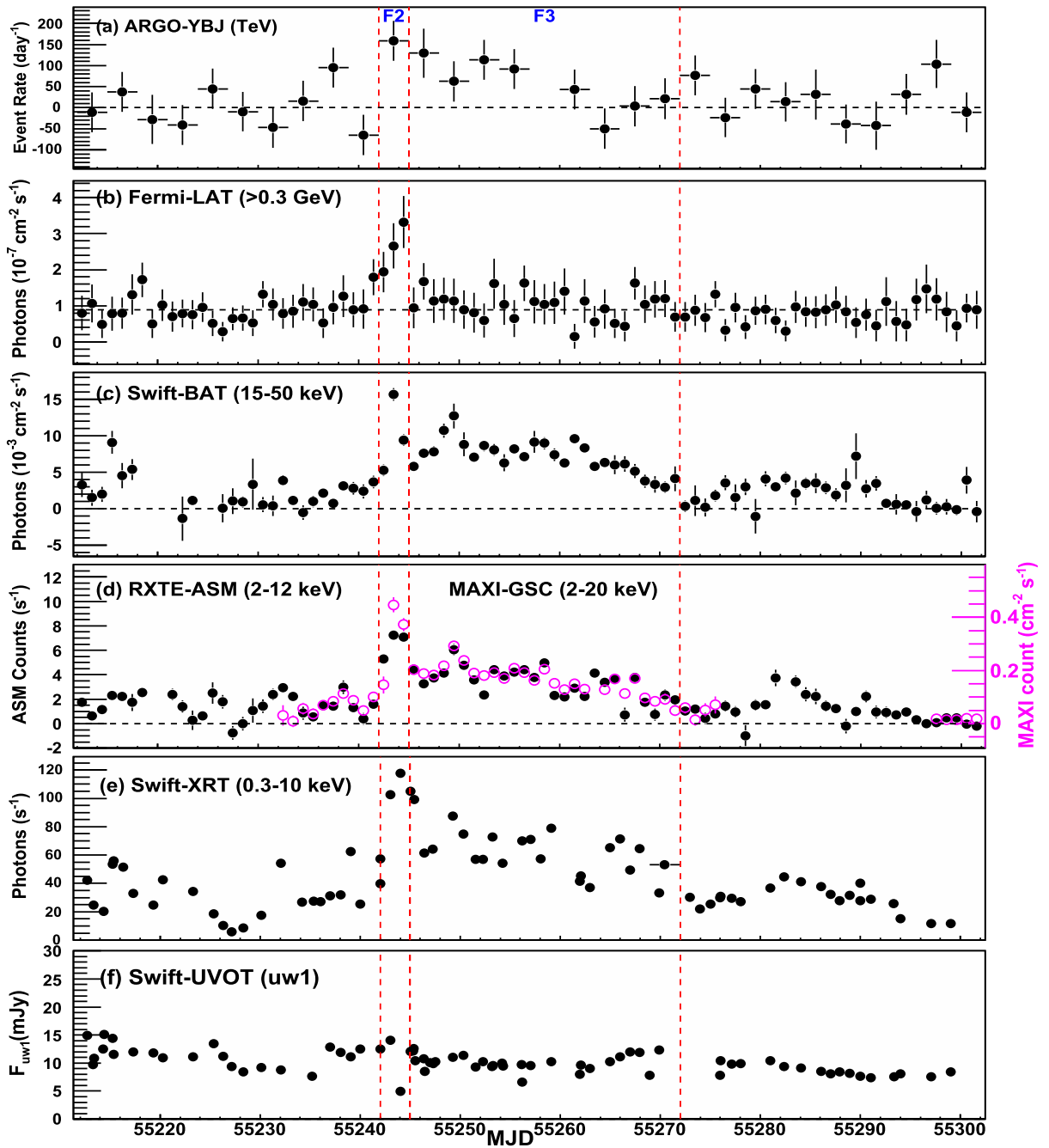


Figure 4. Mrk 421 light curve in different energy bands, from 30 days before Flare 2 to 30 days after Flare 3.

situation, the spectral index is fixed to 3.0. A similar assumption has been chosen for ARGO-YBJ data by fixing the spectral index to 2.75 during F5 and S2. The time-averaged SEDs for the different activity states, obtained by fitting the data of all the experiments, are summarized in Tables 3 and 4. The flux at each energy is shown in Figure 7 and also listed in Table 5. Note that in the following text, the first and the second components refer to the two SED bumps of the SED, as foreseen in the SSC model.

### 3.3.1. Swift-XRT SED

According to the *Swift*-XRT data at 0.3–10 keV, the peak energy of the first component  $E_{peak}$  is  $0.394 \pm 0.003$  keV and

$0.771 \pm 0.003$  keV during S2 and S1, respectively. It increases to  $1.429 \pm 0.004$  keV during the OB phase and even up to 2.4–5.1 keV during F1, F2, and F3. The correlation between the flux and  $E_{peak}$  is shown in Table 4 and Figure 6. A power-law function is adopted to fit their relation, yielding  $f(E_{peak}) = (0.2056 \pm 0.004) \cdot E_{peak}^{-1.266 \pm 0.004} \text{ keV}^{-1} \text{ cm}^{-2} \text{ s}^{-1}$  with  $\chi^2/\text{dof} = 2113/4$ . S1, S2, OB, and F3 roughly follow this function, while F1 and F2 clearly deviate, indicating a different behavior of F1 and F2 with respect to the other flaring states. It is worth noting that the *Swift*-XRT observations during Flare 1 only cover the period with the maximum flux. For this reason, the measured flux is higher than those of *RXTE*-ASM and *MAXI*-GSC, as shown in Figure 7.

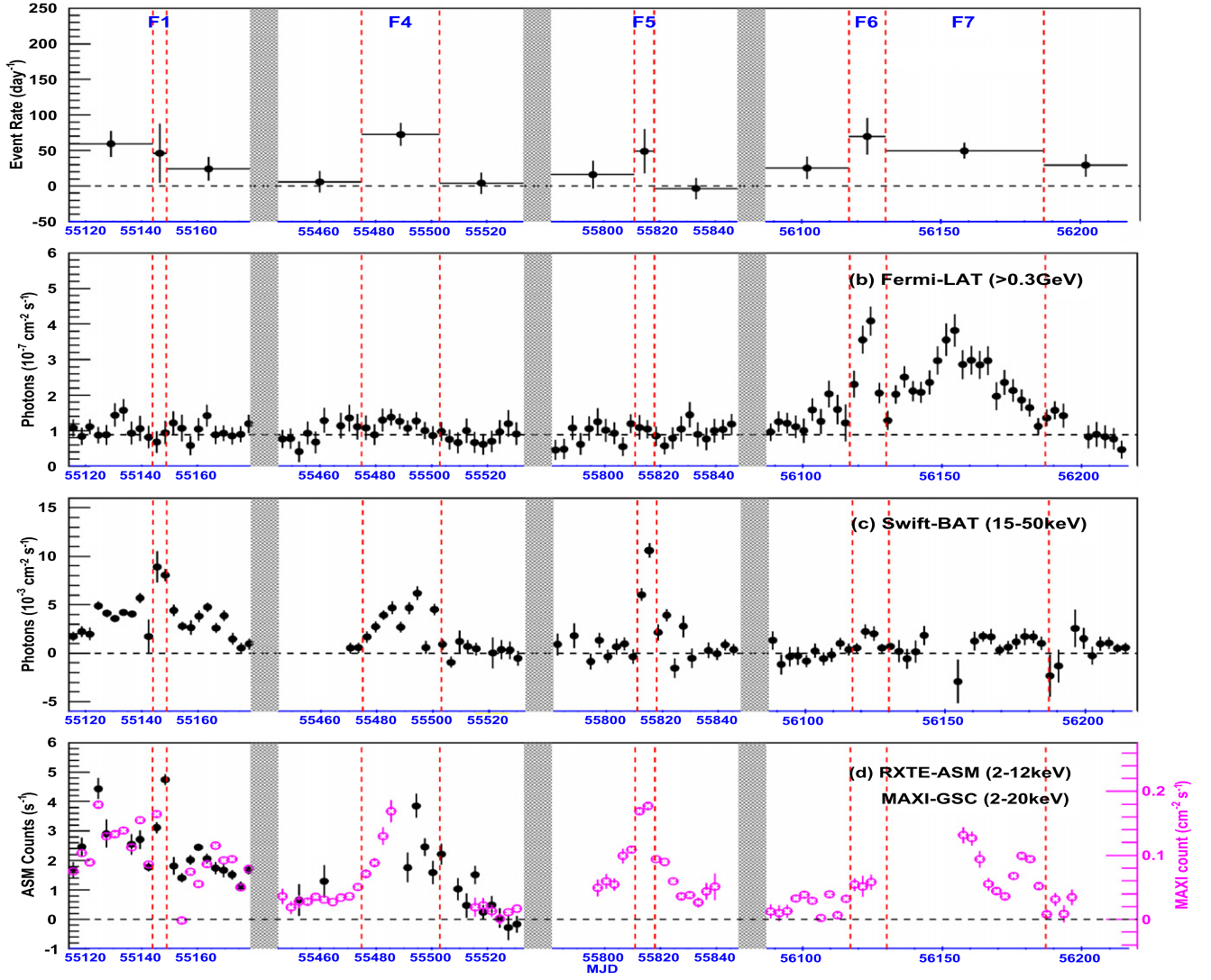


**Figure 5.** Mrk 421 light curve in different energy bands, from 30 days before to 30 days after the 5 flares. Each bin of *Fermi*-LAT, *Swift*-BAT, *RXTE*-ASM, and *MAXI*-GSC contains the event rate averaged over three days.

**Table 3**  
SEDs of Mrk 421 during 10 States (the Unit of the Integral Flux  $F$  is Photons  $\text{cm}^{-2} \text{s}^{-1}$ )

State	MJD	$F_{2-20 \text{ keV}}$ ( $\times 10^{-2}$ )	$\alpha$	$F_{14-195 \text{ keV}}$ ( $\times 10^{-3}$ )	$\alpha$	$F_{0.1-500 \text{ GeV}}$ ( $\times 10^{-7}$ )	$\alpha$	$F_{>1 \text{ TeV}}$ ( $I_{\text{crab}}^a$ )	$\alpha$
Flare 1	55144–55149	$18.3 \pm 1.8$	$2.00 \pm 0.16$	$23.1 \pm 2.6$	$2.78 \pm 0.27$	$1.11 \pm 0.36$	$1.57 \pm 0.15$	$3.2 \pm 0.9$	$2.78 \pm 0.36$
Flare 2	55242–55245	$41.4 \pm 4.2$	$2.38 \pm 0.15$	$19.2 \pm 1.9$	$2.76 \pm 0.18$	$3.48 \pm 0.60$	$1.50 \pm 0.08$	$7.2 \pm 1.5$	$2.61 \pm 0.27$
Flare 3	55245–55272	$19.9 \pm 1.6$	$2.20 \pm 0.11$	$12.9 \pm 0.9$	$2.61 \pm 0.13$	$1.84 \pm 0.21$	$1.79 \pm 0.09$	$1.4 \pm 0.5$	$2.42 \pm 0.46$
Flare 4	55475–55503	$10.0 \pm 1.1$	$2.17 \pm 0.22$	$5.82 \pm 0.83$	$3.02 \pm 0.30$	$2.16 \pm 0.19$	$1.74 \pm 0.05$	$1.9 \pm 0.5$	$2.85 \pm 0.26$
Flare 5	55811–55818	$17.0 \pm 1.6$	$2.13 \pm 0.15$	$13.3 \pm 1.4$	$2.74 \pm 0.23$	$2.23 \pm 0.33$	$1.79 \pm 0.09$	$2.1 \pm 0.8$	$2.75^b$
Flare 6	56117–56130	$6.15 \pm 0.96$	$2.05 \pm 0.35$	$1.45 \pm 0.40$	$2.47 \pm 0.62$	$6.05 \pm 0.39$	$1.68 \pm 0.04$	$1.7 \pm 0.6$	$2.84 \pm 0.39$
Flare 7	56130–56187	$8.70 \pm 0.91$	$2.97 \pm 0.18$	$1.53 \pm 0.36$	$3.09 \pm 0.61$	$5.20 \pm 0.19$	$1.75 \pm 0.02$	$1.1 \pm 0.4$	$3.22 \pm 0.24$
Outburst	55000–55350 <sup>c</sup>	$8.91 \pm 0.74$	$2.41 \pm 0.11$	$4.58 \pm 0.59$	$2.97 \pm 0.23$	$1.92 \pm 0.06$	$1.76 \pm 0.02$	$0.91 \pm 0.14$	$2.67 \pm 0.16$
Steady 1	54683–55000	...	...	$1.50 \pm 0.12$	$2.51 \pm 0.16$	$1.53 \pm 0.05$	$1.75 \pm 0.02$	$0.56 \pm 0.13$	$2.64 \pm 0.27$
Steady 2	55516–56106 <sup>d</sup>	$1.78 \pm 0.18$	$2.38 \pm 0.19$	$0.318 \pm 0.087$	$3.0^b$	$1.69 \pm 0.04^e$	$1.77 \pm 0.01$	$0.33 \pm 0.10$	$2.75^b$
Detector		<i>MAXI</i> -GCS		<i>Swift</i> -BAT		<i>Fermi</i> -LAT		ARGO-YBJ	

**Notes.**

<sup>a</sup>  $I_{\text{crab}} = 1.85 \times 10^{-11}$ .

<sup>b</sup> The spectral index is fixed.

<sup>c</sup> The periods of Flares 1, 2, and 3 have been excluded.

<sup>d</sup> The periods of MJD 55801–55831, including Flare 5, have been excluded.

<sup>e</sup> The flux is  $1.55 \pm 0.04$  assuming a logparabolic spectrum model.

**Table 4**  
SEDs of Mrk 421 During 7 States (the Unit for Integral Flux  $F$  is Photons  $\text{cm}^{-2} \text{s}^{-1}$ )

State	$F_{0.3-10 \text{ keV}}$	a	b	$E_{\text{peak}}$ (keV)	$F_{2-12 \text{ keV}}$ ( $\times 10^{-2}$ )	$\alpha$
Flare 1	$1.227 \pm 0.003$	$1.420 \pm 0.004$	$0.412 \pm 0.008$	$5.06 \pm 0.18$	$18.40 \pm 0.73$	$1.86 \pm 0.08$
Flare 2	$1.251 \pm 0.004$	$1.656 \pm 0.004$	$0.390 \pm 0.009$	$2.76 \pm 0.07$	$27.89 \pm 0.76$	$2.02 \pm 0.06$
Flare 3	$0.903 \pm 0.001$	$1.690 \pm 0.002$	$0.393 \pm 0.003$	$2.48 \pm 0.02$	$13.74 \pm 0.29$	$1.89 \pm 0.04$
Flare 4	...	...	...	...	$10.15 \pm 0.67$	$1.65 \pm 0.12$
Outburst	$0.5746 \pm 0.0003$	$1.864 \pm 0.001$	$0.448 \pm 0.002$	$1.419 \pm 0.004$	$7.19 \pm 0.13$	$2.19 \pm 0.04$
Steady 1	$0.4526 \pm 0.0004$	$2.104 \pm 0.001$	$0.462 \pm 0.003$	$0.771 \pm 0.003$	$4.86 \pm 0.11$	$2.41 \pm 0.06$
Steady 2	$0.229 \pm 0.0003$	$2.352 \pm 0.001$	$0.434 \pm 0.003$	$0.394 \pm 0.003$	$0.68 \pm 0.18$	$2.16 \pm 0.49$
Detector	<i>Swift-XRT</i>			<i>RXTE-ASM</i>		

**Table 5**  
Energy and Flux of the Spectral Points shown in Figures 7 and 8

State	E (TeV)	$E^2 dN/dE$ ( $\text{erg cm}^{-2} \text{s}^{-1}$ )	$\Delta(E^2 dN/dE)$ ( $\text{erg cm}^{-2} \text{s}^{-1}$ )	95% u.l. ( $\text{erg cm}^{-2} \text{s}^{-1}$ )	Detector
S1	4.470e-01	1.698e-11	2.625e-11	6.386e-11	ARGO-YBJ
S1	8.910e-01	3.632e-11	1.494e-11	6.094e-11	ARGO-YBJ
S1	1.413e+00	3.713e-11	9.739e-12	0	ARGO-YBJ
S1	2.818e+00	9.018e-12	6.650e-12	2.024e-11	ARGO-YBJ
S1	4.467e+00	7.560e-12	7.384e-12	2.028e-11	ARGO-YBJ
S1	1.520e-04	2.099e-11	1.840e-12	0	Fermi-LAT
S1	3.080e-04	2.143e-11	1.447e-12	0	Fermi-LAT
S1	6.270e-04	3.193e-11	1.669e-12	0	Fermi-LAT
S1	1.280e-03	3.228e-11	1.963e-12	0	Fermi-LAT
S1	2.590e-03	4.266e-11	2.837e-12	0	Fermi-LAT
S1	5.270e-03	5.517e-11	4.431e-12	0	Fermi-LAT
S1	1.070e-02	5.411e-11	6.199e-12	0	Fermi-LAT
S1	2.180e-02	7.172e-11	1.020e-11	0	Fermi-LAT
S1	4.440e-02	7.453e-11	1.478e-11	0	Fermi-LAT
S1	9.020e-02	9.906e-11	2.503e-11	0	Fermi-LAT
S1	1.830e-01	1.883e-10	5.048e-11	0	Fermi-LAT
S1	3.730e-01	6.174e-11	4.369e-11	1.640e-10	Fermi-LAT
S1	1.800e-08	4.853e-11	3.441e-12	0	Swift-BAT
S1	2.605e-08	3.283e-11	4.348e-12	0	Swift-BAT
S1	3.845e-08	2.889e-11	4.074e-12	0	Swift-BAT

(This table is available in its entirety in machine-readable form.)

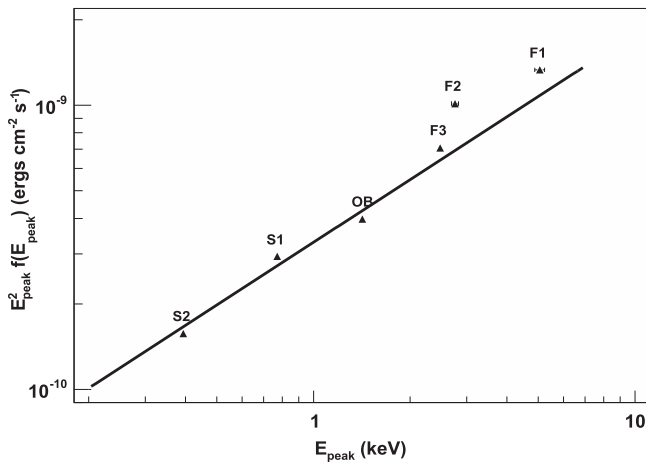


**Figure 6.** Peak energy and the corresponding flux for different Mrk 421 states, as measured by *Swift-XRT* at 0.3–10 keV. The solid line is fitting result using a power-law function, which yields  $f(E_{\text{peak}}) = (0.2056 \pm 0.004) \cdot E_{\text{peak}}^{-1.266 \pm 0.004} \text{ keV}^{-1} \text{ cm}^{-2} \text{ s}^{-1}$  with  $\chi^2/\text{dof} = 2113/4$ .

### 3.3.2. MAXI-GSC and Swift-BAT SEDs

According to *MAXI-GSC* measurements at 2–20 keV, the flux during the flaring periods increases by about a factor 4–20, compared to S2. The spectral indexes for most of the states are in the 2–2.4 range while the spectrum softens (index  $2.97 \pm 0.18$ ) during F7. In the X-ray band (14–195 keV), the *Swift-BAT* data shows an even larger variation (4–70 times) with spectral indexes ranging from 2.5 to 3.1.

### 3.3.3. Fermi-LAT and ARGO-YBJ SEDs

As stated in Section 2, we also test the significance of the spectrum curvature in the *Fermi-LAT* data. During the S2 phase, the  $\text{TS}_{\text{curve}}$  value is found to be 32.6, corresponding to 5.7 standard deviations (s.d.). An evidence for a curvature is then observed in S2, with a peak energy  $E_{\text{peak}} = (60 \pm 11)$  GeV. The  $\text{TS}_{\text{curve}}$  values for F2 and F7 are 8.0 and 9.4, respectively, corresponding to 2.8 and 3.1 s.d., only showing a hint of curvature. The  $\text{TS}_{\text{curve}}$  values for the other seven states

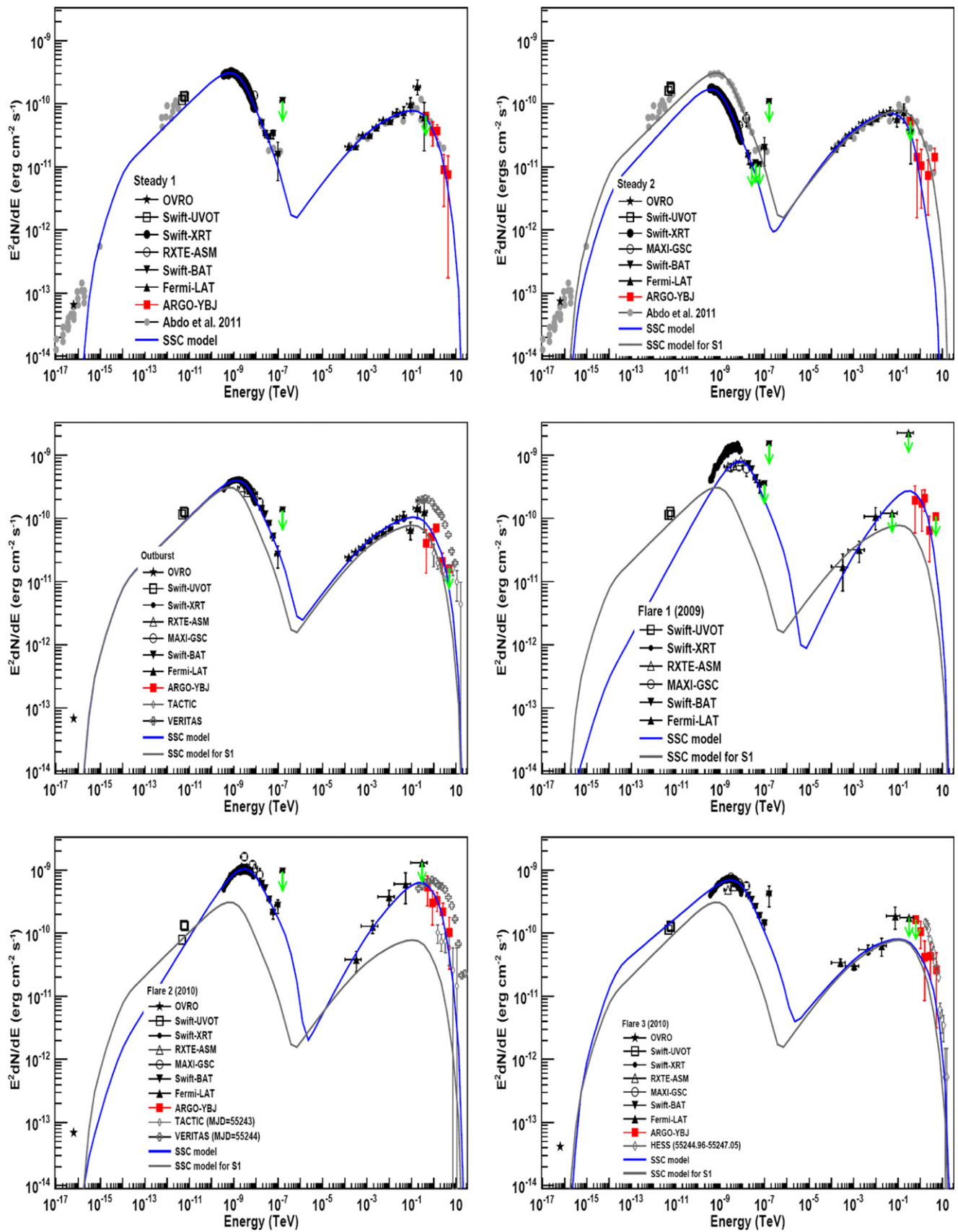


**Figure 7.** Spectral energy distribution of Mrk 421 during 10 states. The solid line shows the best fit to the data, assuming a homogeneous one-zone SSC model (the best-fit parameters are listed in Table 6). For comparison, the model describing the Steady 1 (S1) is also plotted in the other nine states.

are less than 3.4. No curvature are detected in these cases. These features are visible in Figure 7. Note that the data points of *Fermi*-LAT are the result of the analysis made in differential energy ranges, and are independent of the assumed spectral models.

In the GeV  $\gamma$ -ray band, the F3, F4, F5, OB, S1, and S2 phases have similar spectral indexes (ranging from 1.74 to 1.80) and fluxes (within 32%), as shown in Table 3. Compared to the S2 state, the spectral index of F1 shows a moderate hardening ( $\Delta\alpha = 0.20 \pm 0.15$ ) and a flux decrease of  $(34 \pm 21)\%$ . The spectral index of F2 hardens more significantly ( $\Delta\alpha = 0.27 \pm 0.08$ ) with a flux increase of a factor  $2.06 \pm 0.36$ . A flux enhancement by a factor 3 is observed during F6 and F7, with a harder spectral index during F6 ( $\Delta\alpha = 0.09 \pm 0.04$ ) and a negligible index variation during F7.

In VHE  $\gamma$ -ray band, the S2 flux is estimated to be  $(0.33 \pm 0.10) I_{\text{crab}}$ , assuming a fixed spectral index,  $\alpha = 2.75$ . This result is comparable to the baseline flux of Mrk 421 obtained using a 20 year long-term combined ACT data (Tluczykont et al. 2010), which is estimated to be less than  $0.33 I_{\text{crab}}$  above 1 TeV. The averaged measured flux is  $(0.56 \pm 0.13)$  and  $(0.91 \pm 0.14) I_{\text{crab}}$  during S1 and OB phase, respectively. F2 is the largest flare, achieving a flux of  $(7.2 \pm 1.5) I_{\text{crab}}$ . The flux of the remaining flares is around  $(1-3) I_{\text{crab}}$ . The spectral index of F7 ( $\alpha = 3.22 \pm 0.24$ ) marks the softest spectrum of the observed flares. The flux modulations appears in coincidence with the X-ray observations.

Summarizing the above results, we can conclude that the flux enhancements are detected in both X-rays and VHE  $\gamma$ -rays during all the nine states, compared to the baseline S2. The behavior in the GeV band is actually different. Accordingly, a phenomenological classification of three types of SEDs (T1, T2, and T3) is here introduced: (1) flares with no or little GeV flux and photon index variations, (2) flares with  $\gamma$ -ray spectral hardening, irrespective of the flux variations, and (3) flares with flux enhancements, irrespective of spectral behavior. Type T1 includes phases S1, S2, F3, F4, F5, and OB. Type T2 includes the F1 and F2 states and also the day (MJD = 56124), corresponding to the F6 maximum flux, during which the spectral index significantly hardens to  $\alpha = 1.60 \pm 0.04$ . It is worth noting that this variation is fast: the hardening phase only lasts two days and recovers soon, indicating an unstable state. Type T3 includes phases F6 and F7. Actually, the spectral index of F7 becomes softer above the peak energy for both low- and high-energy components. The previous flare on 2008 May 7, reported by Acciari et al. (2009b), not included in this present discussion, may also belong to this type.

During flares of types T1 and T2, the peak energies of both the low- and high-energy components shift to higher energy with respect to the baseline state S2. This tendency is consistent with most of the previous measurements (Massaro et al. 2008; Albert et al. 2007) based on fragmented observations. This indicates that the modulation of Mrk 421 flux follows these types in most of the cases. During flares of type T3, the peak energies could shift to lower energy with respect to S2, but this must be determined by the future observations of similar flares.

### 3.4. Cherenkov Detectors VHE $\gamma$ -ray Data

During the 4.5 year period from 2008 August to 2013 February, Cherenkov detectors (e.g., VERITAS, MAGIC) also

observed Mrk 421 in the VHE band. Even if these detectors cannot monitor Mrk 421 day by day, they can provide more precise measurements for short periods, due to their excellent sensitivity.

To give an example of the timing coverage of a Cherenkov detector, a dummy instrument located at  $30^\circ$  N (close to the latitude of VERITAS,  $32^\circ$  N, and MAGIC,  $28^\circ$  N) is here considered to estimate the allowable observation time for Mrk 421. Figure 9 shows the allowable time, requiring the Sun zenith angle be greater than  $105^\circ$ , the moon zenith angle greater than  $100^\circ$ , and the Mrk 421 zenith angle less than  $50^\circ$ .

Among the seven flares presented in the last section, F4, F5, F6, and F7 occurred during the period from July to October, forbidden for Cherenkov detector observations, since Mrk 421 is close to the direction of the Sun. The moonlight completely hampered Cherenkov telescope observations during F1 and partially during F3. Only flare F2 could be eventually observed every night by Cherenkov detectors.

Actually, VERITAS observed Mrk 421 during the last day of F2, i.e., MJD = 55244. The preliminary spectrum is shown in Figure 7 and the corresponding flux above 1 TeV is  $16.8 I_{\text{crab}}$  (Fortson 2012). TACTIC observed Mrk 421 every night during F2 (Singh et al. 2015). The peak flux measured on February 16 (MJD = 55243) and the corresponding spectrum during the peak flux day is also shown in Figure 7. The flux above 1 TeV is  $2.7 I_{\text{crab}}$ . HAGAR also observed Mrk 421 every night during F2 (Shukla et al. 2012). The peak flux on February 17 (MJD = 55244) is about  $7 I_{\text{crab}}$ . It is worth recalling that the average flux detected by ARGO-YBJ during the three days of F2 is  $(7.2 \pm 1.5) I_{\text{crab}}$ .

Both VERITAS and HESS observed the first three days of flare F3. VERITAS preliminary results show that the flux decreased from  $5.7 I_{\text{crab}}$  to  $2.9 I_{\text{crab}}$  (Fortson 2012). HESS preliminary results also shows a decreasing flux from 4.8 to  $1.4 I_{\text{crab}}$  (Tluczykont 2011).

The S1 period extends over the years 2008–2009 and during this time the Whipple telescope monitored the Mrk 421 emission. The total observation time is 130.6 hr and the mean  $\gamma$ -ray rate is  $0.55 \pm 0.03 I_{\text{crab}}$  (Acciari et al. 2014), which is consistent with the ARGO-YBJ result, i.e.,  $0.56 \pm 0.13 I_{\text{crab}}$ . During this period, MAGIC also observed Mrk 421 for about 27.7 hr (Abdo et al. 2011; Aleksic et al. 2015a). The photon fluxes for the individual observations gave an average flux of about 50% that of the Crab Nebula, with relatively mild (typically less than a factor of two) flux variations. The spectrum, shown in Figure 7, is consistent with the ARGO-YBJ data.

The OB period lasts over the years 2009–2010. The spectrum measured by TACTIC, shown in Figure 7, is lower than that by ARGO-YBJ. The preliminary spectrum reported by VERITAS (Galante 2011) is also shown in Figure 7, which is higher than the one of ARGO-YBJ. These differences may be caused by the different observation times, considering that Mrk 421 was in an active and variable phase.

## 4. THE SSC MODEL FOR MRK 421

The different types of Mrk 421 flux variations can be associated with the intrinsic astrophysical mechanisms of the emission. In the following, we will investigate the major parameters correlated to these variations in the framework of the one-zone SSC emission model.

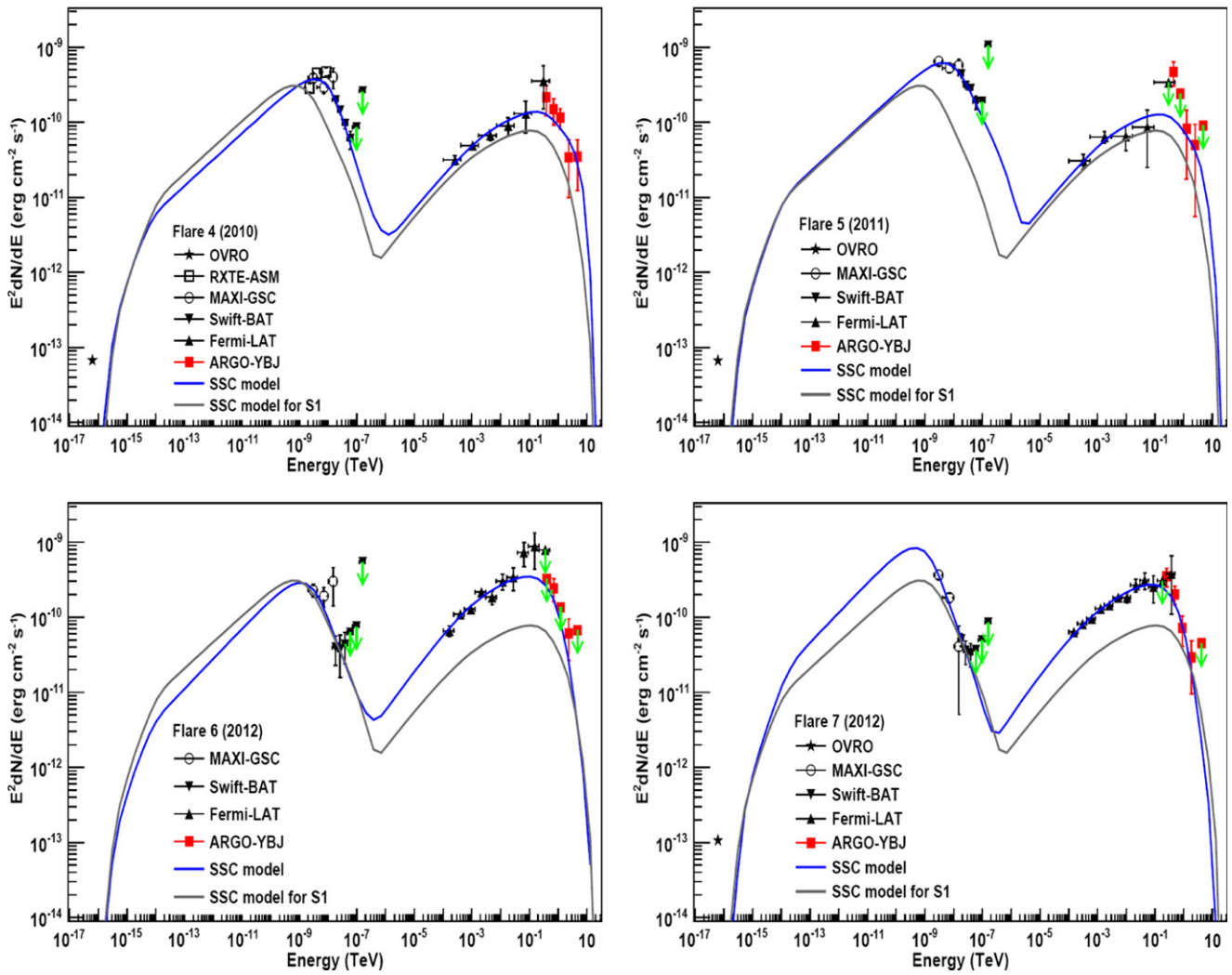


Figure 8. Continuation of Figure 7.

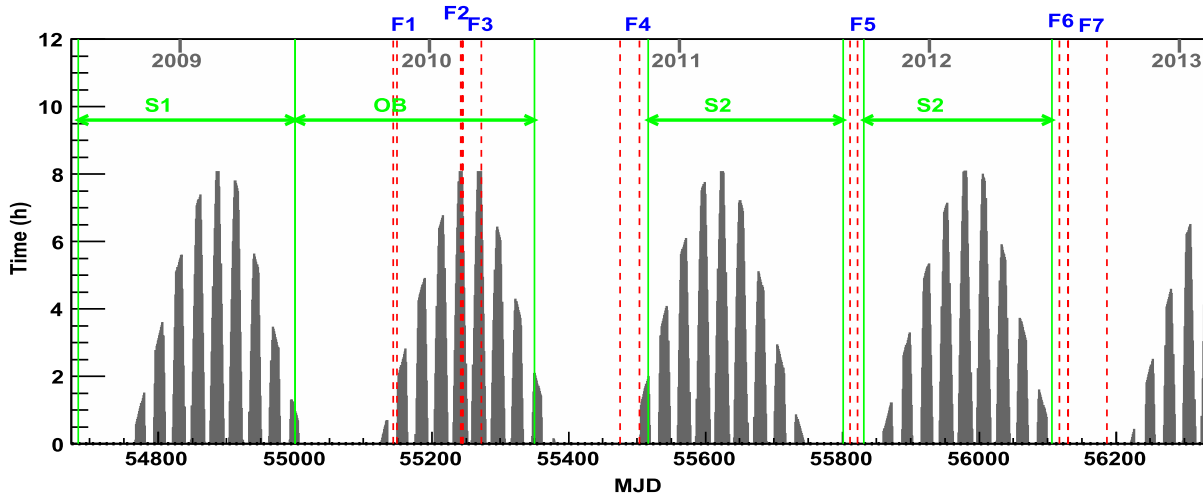


Figure 9. Daily allowable Mrk 421 observation time for a Cherenkov detector located at  $30^\circ$  north of latitude, during the 4.5 years considered in this work.

In this paper, the one-zone homogeneous SSC model proposed by Krawczynski (2004) is adopted to fit the multi-wavelength SEDs measured during different states. In this model, a spherical blob of plasma with a comoving radius  $R$  is assumed. The relativistic Doppler Factor of the emitting plasma

is defined as  $\delta = [\Gamma(1 - \beta \cos\theta)]^{-1}$ , where  $\Gamma$  is the bulk Lorentz factor of the emitting plasma,  $\beta$  is its bulk velocity in units of the speed of light, and  $\theta$  is the angle between the jet axis and the line of sight, as measured in the observer frame. The emission volume is filled with an isotropic population of

**Table 6**  
Best-Fit Parameters in the SSC Model for 10 States

State	$p_1$	$p_2$	$\log(E_{\text{break}})$ (eV)	$\delta$	B (G)	$u_e$ ( $10^3 \text{ erg cm}^{-3}$ )	$u_e/u_B^a$	$W_e^b$ ( $10^{46} \text{ erg}$ )	$\chi^2_\gamma/\text{ndf}$	$\chi^2_{\text{all}}/\text{ndf}$
Steady 1	$2.30^{+0.06}_{-0.04}$	$4.70^{+0.07}_{-0.03}$	$11.00^{+0.04}_{-0.03}$	$38^{+6}_{-4}$	$0.048^{+0.012}_{-0.012}$	$6.65^{+0.15}_{-0.15}$	70.6	2.8	23.0/11	238/501
Steady 2	$2.22^{+0.09}_{-0.06}$	$4.68^{+0.02}_{-0.04}$	$10.78^{+0.05}_{-0.04}$	$15^{+4}_{-2}$	$0.17^{+0.07}_{-0.05}$	$12.7^{+0.4}_{-0.5}$	10.6	5.3	13.2/11	236/467
Outburst	$2.30^{+0.08}_{-0.05}$	$4.51^{+0.03}_{-0.02}$	$11.13^{+0.02}_{-0.05}$	$35^{+3}_{-3}$	$0.054^{+0.026}_{-0.005}$	$7.74^{+0.24}_{-0.14}$	65.7	3.2	23.5/12	600.8/643
Flare 1	$1.7^{+0.3}_{-0.3}$	$4.7^{+1.2}_{-0.5}$	$11.51^{+0.09}_{-0.03}$	$10^{+2}_{-2}$	$0.14^{+0.07}_{-0.04}$	$31^{+7}_{-5}$	41.3	12.9	1.6/2	7.3/14
Flare 2	$1.85^{+0.20}_{-0.20}$	$4.30^{+0.05}_{-0.12}$	$11.27^{+0.03}_{-0.03}$	$17^{+3}_{-2}$	$0.092^{+0.028}_{-0.024}$	$24^{+2}_{-2}$	73.0	10.1	3.7/3	179/308
Flare 3	$2.40^{+0.15}_{-0.15}$	$4.60^{+0.08}_{-0.09}$	$11.21^{+0.02}_{-0.03}$	$41^{+5}_{-3}$	$0.080^{+0.011}_{-0.017}$	$4.40^{+0.07}_{-0.10}$	17.3	1.8	13.2/4	1055.7/574
Flare 4	$2.30^{+0.15}_{-0.15}$	$5.6^{+0.9}_{-0.6}$	$11.49^{+0.08}_{-0.07}$	$35^{+10}_{-7}$	$0.033^{+0.019}_{-0.013}$	$12.3^{+1.3}_{-1.0}$	289.2	5.2	6.1/5	23.4/15
Flare 5	$2.3^{+0.4}_{-0.2}$	$4.6^{+0.7}_{-0.5}$	$11.35^{+0.13}_{-0.12}$	$31^{+21}_{-13}$	$0.072^{+0.108}_{-0.047}$	$8.0^{+1.4}_{-1.2}$	39.2	3.4	6.8/4	12.1/13
Flare 6	$2.20^{+0.11}_{-0.17}$	$5.1^{+1.8}_{-0.7}$	$11.17^{+0.24}_{-0.43}$	$15^{+24}_{-5}$	$0.085^{+0.053}_{-0.033}$	$40^{+28}_{-30}$	120.8	16.8	12.1/8	17.5/17
Flare 7	$2.20^{+0.12}_{-0.07}$	$5.2^{+0.3}_{-0.2}$	10.78	$30^{+7}_{-5}$	$0.115^{+0.038}_{-0.032}$	$8.77^{+1.40}_{-1.32}$	16.6	3.7	2.45/3	14.1/20

**Notes.**

$$^a u_e/u_B = 8\pi u_e/B^2.$$

$$^b W_e = u_e \frac{4}{3} \pi R^3.$$

electrons and a randomly oriented uniform magnetic field  $B$ . The SED of the injected electrons in the jet frame is assumed to follow a broken power law with indexes  $p_1$  and  $p_2$  below and above the break energy  $E_{\text{break}}$ . The electron distribution is normalized by a factor  $u_e$  (in units of  $\text{erg cm}^{-3}$ ). To reduce the free parameters in the model, the low limit for the electron energy  $E_{\text{min}}$  is fixed to be  $500 \cdot m_e c^2$  and the high limit  $E_{\text{max}}$  is assumed to be  $10 \cdot E_{\text{break}}$ . The radius of the emission zone is constrained by the variability of the timescale as  $R < ct_{\text{var}}\delta/(1+z)$ . In the multi-wavelength data considered in this analysis, the fastest variability has a timescale of  $\sim 1$  day, observed during F2, in X-rays and GeV  $\gamma$ -rays, as shown in Figure 4. In this work, the radius  $R$  for all phases are arbitrarily set to be  $10^{14}$  m, being  $t_{\text{var}} > 4.8(20/\delta)$  hr the allowed time variability range. So far we have still six free parameters:  $p_1$ ,  $p_2$ ,  $E_{\text{break}}$ ,  $u_e$ ,  $B$ , and  $\delta$  to be determined experimentally by fitting the data presented in Figure 7.

In this work, we use the least-square method to determine the best values of the parameters  $p_1$ ,  $p_2$ ,  $E_{\text{br}}$ ,  $B$ ,  $\delta$ , and  $u_e$ . For the *Swift*-XRT flux data, we added a 3% systematic error besides the statistical error listed in Table 5. The ultraviolet and radio data points were not used for the fit, as will be discussed later. The extragalactic background light (EBL) absorption of the VHE  $\gamma$ -ray is included in the calculation, according to the Franceschini et al. (2008) model.

Since the parameter  $p_1$  is related to the spectral shape at energies below the synchrotron and inverse Compton peaks, it is mainly determined by the *Swift*-XRT data in X-rays and by the *Fermi*-LAT data in GeV  $\gamma$ -rays. For 5 out of 10 states, the *Swift*-XRT data around the synchrotron peak are not available. Therefore, in these cases,  $p_1$  is mainly determined by the *Fermi*-LAT data. The synchrotron peak energies of states S1 and S2 are close to the low-energy limit of the *Swift*-XRT data, hence the measurement below the synchrotron peak cannot strongly constrain the  $p_1$  value, which, in this case, will also be

mainly determined by the *Fermi*-LAT data. For the remaining three states, the statistical accuracy of the *Swift*-XRT data is much better than that of other detectors; however, the low-energy *Swift*-XRT measurements (at energies below  $\sim 1$  keV) are biased by the uncertainty in the absorption of hydrogen-equivalent column density and by detector systematics<sup>32</sup> (such as the CCD charge trapping, generated by radiation and high-energy proton damage, affecting mostly the low-energy events). For this reason, we prefer to use only  $\gamma$ -ray data for all the 10 states when fitting the parameter  $p_1$ . The result and chi squares ( $\chi^2_\gamma/\text{ndf}$ ) obtained by the fitting procedure are listed in Table 6. The derived  $p_1$  values for type T1 and T3 states are consistent within errors, ranging from 2.2 to 2.4. The results for T2 flares indicate a harder electron spectrum, with  $p_1 = 1.7 \pm 0.3$  for F1 and  $p_1 = 1.85 \pm 0.20$  for F2.

To obtain the remaining five parameters, the entire SED data above 0.3 keV are used. The *Swift*-XRT observation during F1 is not taken into account. The parameter  $p_2$  is determined by the spectral shape above the synchrotron and inverse Compton peak energies. Therefore, the parameter  $p_2$  is mainly determined by the *Swift*-XRT, *RXTE*-ASM, *MAXI*-GSC, and *Swift*-BAT data in X-rays, and by the ARGO-YBJ data in TeV  $\gamma$ -rays. The accuracy of the *Swift*-XRT measurements is much higher than that of other detectors; therefore,  $p_2$  can be well determined for states in which *Swift*-XRT data are available. The parameter  $\delta$  is mainly determined by both the synchrotron and inverse Compton peak energies. There are no data around the synchrotron peak for F5, F6, and F7; therefore, in these cases  $\delta$  cannot be well constrained. In particular, we cannot find a best value for F7 within a reasonable range. For flare F7, we arbitrarily set the value of  $E_{\text{break}}$  equal to the one derived for the S2 state.

<sup>32</sup> <http://heasarc.gsfc.nasa.gov/docs/heasarc/caldb/swift/docs/xrt/>

According to the fit results, the SSC model reasonably describes all the SEDs, as shown in Figures 7 and 8. The fact that *Swift*-XRT data below 0.5 keV are not perfectly described during OB, F2, and F3 may be explained by the systematic errors previously discussed. The obtained parameters and chi squares ( $\chi_{\text{all}}^2/ndf$ ) are summarized in Table 6. The Doppler factor  $\delta$ , ranging from 10 to 41, is similar to the ones found in previous investigations (Abdo et al. 2011; Bartoli et al. 2011a; Shukla et al. 2012; Zhang et al. 2012). The values of the magnetic field,  $B \sim 0.1$  G, are almost constant within a factor 2. The jet power in electrons ( $10^{46}$ – $10^{47}$  erg) is much higher than that in magnetic field, as indicated by the electron energy density to the magnetic field energy density ratio  $u_e/u_B$ , listed in Table 6.

## 5. DISCUSSION

Using the long-term multi-wavelength data from radio to VHE  $\gamma$ -rays, we have shown that Mrk 421 is active at all wavebands during the 4.5 years considered in this work. The variability of Mrk 421 increases with energy for both the low- and high-energy SED components. The source is highly variable in the X-ray and VHE  $\gamma$ -ray bands, with the normalized variability amplitudes greater than 70% (see Figure 3). An overall cross-correlation analysis (see Table 2) between the *Swift*-BAT and ARGO-YBJ data shows that the variabilities in X-rays and VHE  $\gamma$ -rays are generally correlated. The correlation is also clearly visible in the light curves during the large X-ray flares (see Figures 2, 4 and 5). Our previous observations during the outburst of 2008 also show that X-rays and VHE  $\gamma$ -rays were tightly correlated with the peak times in good agreement with each other (Bartoli et al. 2011a). A clear correlation between the X-rays and VHE  $\gamma$ -rays has also been reported in many observations in the past decades (Blazewski et al. 2005; Chen 2013; Acciari et al. 2014). All these results firmly support the idea that the X-ray and VHE  $\gamma$ -ray emissions of Mrk 421 originate from the same zone.

The variability amplitude in GeV  $\gamma$ -rays is 39% (see Figure 3), which is less than that in VHE  $\gamma$ -rays. In fact, the amplitude of the GeV  $\gamma$ -ray variability is very low most of the time, being only about 20% if the large GeV  $\gamma$ -ray flares F6 and F7 are excluded. The overall cross-correlation analysis (see Table 2) shows that GeV  $\gamma$ -rays are moderately correlated with VHE  $\gamma$ -rays. The GeV and VHE  $\gamma$ -ray light curves reported in Figures 4 and 5 show an evident correlation only during F2, F6, and F7. According to the measurements shown in Table 3, during flares F3, F4, F5, and the OB phase, the flux above 0.1 GeV increases by 20%–46% with respect to the S1 steady state, while the VHE flux increases by 63%–275%. With these results, we could not exclude the possibility that GeV and TeV  $\gamma$ -rays are produced in different emission zones. A possible scenario would be that the observed emission is the superposition of one stationary zone with a steady GeV emission and one active zone responsible for the VHE flux variation (e.g., Cao & Wang 2013; Aleksic et al. 2015b). However, during flares F1, F2, F6, and F7, GeV and TeV  $\gamma$ -rays show clear correlated variations, according to the SEDs reported in Figure 7. This could indicate that GeV and TeV emissions are generated in the same zone, at least during these phases. In particular, during flare F1, the flux above 0.1 GeV decreases by about  $(27 \pm 24)\%$ . If this decrease is not due to a statistical fluctuation, the stationary zone would be excluded, and the above hypothesis of two emission zones could be excluded,

too. Moreover, during F6 and F7, the GeV  $\gamma$ -ray flux increases by a large amount (240%–295%), while the spectral indices were about consistent. Also, this result does not support the hypothesis of two zones, since the predicted spectrum at GeV energies for the active zone is much harder than that for the steady zone, according to Cao & Wang (2013) and Aleksic et al. (2015b).

Compared to other wavebands, the flux variation at radio frequencies is much weaker. A radio flare is observed in 2012, which is the largest radio flare ever observed in Mrk 421 (Hovatta et al. 2015). The cross-correlation analysis shows that this radio flare follows the GeV  $\gamma$ -ray flare with a time lag of about 42 days (see Table 2), which is consistent with Hovatta et al. (2015). If the radio and GeV  $\gamma$ -ray flares are physically connected (Hovatta et al. 2015), then the GeV  $\gamma$ -ray emission could originate upstream of the radio emission. The distance between radio and GeV  $\gamma$ -ray emission sites and their distances to the central black hole have been discussed by Max-Moerbeck et al. (2014).

The variability amplitude in the UV band is 33%, similar to that in GeV  $\gamma$ -rays. However, according to the cross-correlation analysis (see Table 2) and to the light curves (see Figures 2 and 4), the UV flux does not appear to be correlated with GeV  $\gamma$ -rays. The UV flux does not even show an evident correlation with X-rays. Moreover, according to the SED of flare F1 shown in Figure 7, the UV and X-ray data cannot be fitted together with a unique component. These results seem to indicate that the UV and X-ray emissions do not share the same origin. Instead, the moderate correlation observed between UV and radio suggests that their emission regions could be the same, possibly located downstream of the X-ray and  $\gamma$ -ray emission zone. Therefore, the radio and UV data points were removed from the SSC model fitting. This choice is different from other authors, e.g., Abdo et al. (2011) and Shukla et al. (2012), who included them when fitting the SED. Finally, the SSC model generally underpredicts the UV and radio emissions. This supports our hypothesis that, at least partially, the radio and UV emission comes from regions in the jet not emitting X-rays and  $\gamma$ -rays.

For the type T1 and T3 states, the derived spectral indices  $p1$  are generally consistent with  $p1 = 2.2$ , i.e., the canonical particle spectral index predicted for relativistic diffuse shock acceleration (for a review, see Kirk & Duffy 1999). This suggests that this process is active in Mrk 421. The change of the electron index  $\Delta p = p2 - p1$  is larger than the expected typical cooling break  $\Delta p = 1$  (Kino et al. 2002), indicating that the break is not induced by radiative cooling. The cooling mechanism may be less important, as suggested in Acciari et al. (2011). Abdo et al. (2011) speculated that the steep break is a characteristic of the acceleration process which is not yet understood. The break energy  $E_{\text{break}}$  should represent the maximum energy that can be achieved in the acceleration process, depending on the acceleration time of the particle in the shock area. Accordingly, the flares of T1 type should be mainly caused by the variation of the maximum energy of the electrons reached within the shock area. Concerning the type T3 flares (i.e., F6 and F7), these flares might be due to the increase of the magnetic field ( $B$ ) or comoving particle density ( $u_e$ ) compared to S1.

Up to now, it is not yet clear how shocks work in a jet. If the different states detected in this work are caused by different shocks, we could expect different features of emission zones,

such as  $B$ ,  $\delta$ ,  $R$ , electron density, and spectrum. If the different states are caused by similar shocks moving down the jet, we would expect emission zones with the same  $R$ , for all the states, as we assumed when fitting the SED using the SSC model. In such a hypothesis, we could guess that the underlying mechanism responsible for the flares of T1 and T3 types may be due to the variation of the ambient medium. In the theory of diffusive acceleration, the acceleration timescale of particles is related to the strength of the magnetic field both in the upstream and downstream regions (Drury 1983). The upstream magnetic field could be related to the ambient medium. The variation of the acceleration timescale may change the maximum energy of the particles achieved within the shock. When the density and the magnetic field of the ambient medium are different, the number of particles and the corresponding maximum energy can be different. In such a hypothesis, the variability timescale for each state would characterize the size of each medium block that is crossed by the shock.

The T2 flares require a harder injected electron spectrum than the other types. This change would be caused by the acceleration processes. The slopes of F1 and F2 go beyond the predictions of a spectral index of 2.0 given by the canonical non-relativistic diffuse shock acceleration. According to Stecker et al. (2007), particle spectra with spectral indexes less than 2 can be realized within the relativistic shock using extreme parameters, i.e., large scattering angles. F1 and F2 flares only last a few days, which means that the produced electrons with spectral index less than 2.2 is a transient state and cannot last for a long time. So, we cannot exclude the possibility that such short flares are due to extreme parameters. Another alternative mechanism for such a hard spectrum would be that the particles accelerated by the shock are subsequently accelerated by the stochastic process in the downstream region, which is able to produce spectra that are significantly harder than the limits of the first-order mechanism within a short time (Virtanen & Vainio 2005). Recently, Guo et al. (2014) also predicted a hard spectral index resulting from relativistic magnetic reconnection.

## 6. SUMMARY

In this paper, we have presented a 4.5 year continuous multi-wavelength monitoring of Mrk 421, from 2008 August 5 to 2013 February 7, a period that includes both steady states and episodes of strong flaring activity. The observations concern a wide energy range, from radio to TeV  $\gamma$ -rays. In particular, due to the ARGO-YBJ and *Fermi* data, the entire energy range from 100 MeV to 10 TeV is covered without any gap. These extensive data sets are essential for studying the origin of the flux variability and to investigate the underlying emission mechanism. The main results of this work can be summarized as follows.

1. Mrk 421 showed both low- and high-activity phases at all wavebands during the 4.5 year period analyzed in this work. The variability increases with energy for both the SED components. Concerning the synchrotron component, the variability amplitude increases from 21% in radio and 33% in UV to 71%–73% in soft X-rays and 103%–137% in hard X-rays. For the inverse Compton component, the amplitude is 39% at GeV energies and increases to 84% at TeV energies.
2. The time correlation among the flux variation in different wavebands was analyzed. The variation of the X-ray flux is clearly correlated with the TeV  $\gamma$ -ray flux. This result is consistent with many previous observations in the past decades, supporting the idea that the X-ray and VHE  $\gamma$ -ray emissions originate from the same zone. The GeV  $\gamma$ -ray flux appears to be moderately correlated with the TeV  $\gamma$ -ray flux. This result is new compared to previous results. The correlation is mainly due to the large GeV  $\gamma$ -ray flares occurred in 2012 and a large X-ray/TeV  $\gamma$ -ray flare in 2010. Taking into account the spectral shape during these flares, we can conclude that the GeV and TeV  $\gamma$ -rays also originate from the same zone, at least during these flares. On the contrary, X-ray and  $\gamma$ -ray fluxes are weakly or not correlated with radio and UV fluxes.
3. According to the observed light curves, 10 states (2 steady periods, S1 and S2, 1 outburst period, OB, and 7 large flares) have been selected and analyzed. Five flares have been identified in X-rays, and two in GeV  $\gamma$ -rays. The duration of the flares ranges between 3 and 58 days. X-ray and TeV  $\gamma$ -ray fluxes increase during all the active states. In X-rays, the flux increases by a factor 4–70 and the peak energy increases from 0.4 keV to 1.4–5.1 keV. At TeV energies, the flux has been observed to vary from  $0.33 I_{\text{crab}}$  to  $7 I_{\text{crab}}$ .
4. According to the behavior of GeV  $\gamma$ -rays, the activity states can be classified into three groups. (1) flares with no or little GeV flux and photon index variations, e.g., S1, S2, OB, F3, F4, and F5; (2) flares with  $\gamma$ -ray spectral hardening, irrespective of the flux variations, e.g., F1 and F2; (3) flares with flux enhancements, irrespective of spectral behavior, e.g., F6 and F7.
5. A simple one-zone SSC model is adopted to fit the multi-wavelength SED state by state. The SSC model can satisfactorily reproduce all the SED measurement except the *Swift*-XRT data below 0.5 keV, probably due to a detector systematics affecting the low-energy events. For type I and III states, the derived injected electron spectral indices are around 2.2, as expected from relativistic diffuse shock acceleration, indicating that this process can be active in Mrk 421. According to the derived parameters, the variation of these states may be caused by the variation of environment properties. Instead, type II flares require harder injected electron spectra, with spectral indices around 1.7–1.9. The underlying physical mechanisms responsible for this type of flares may be related to the acceleration process itself.

This work is supported in China by NSFC (No.11205165, No.11575203, No.11375210), the Chinese Ministry of Science and Technology, the Chinese Academy of Sciences, the Key Laboratory of Particle Astrophysics, CAS, and in Italy by the Istituto Nazionale di Fisica Nucleare (INFN). We are grateful to Dahai Yan and Liang Chen for their helpful suggestions that improved the paper. We also acknowledge the essential supports of W.Y. Chen, G. Yang, X.F. Yuan, C.Y. Zhao, R. Assiro, B. Biondo, S. Bricola, F. Budano, A. Corvaglia, B. D’Aquino, R. Esposito, A. Innocente, A. Mangano, E. Pastori, C. Pinto, E. Reali, F. Taurino, and A. Zerbini in the installation, debugging, and maintenance of the detector of ARGO-YBJ. This research has made use of data and software

provided by the High Energy Astrophysics Science Archive Research Center (HEASARC), which is a service of the Astrophysics Science Division at NASA/GSFC and the High Energy Astrophysics Division of the Smithsonian Astrophysical Observatory. We acknowledge the use of the ASM/*RXTE* quick-look results provided by the ASM/*RXTE* team, the MAXI data provided by RIKEN, JAXA and the MAXI team, Swift/BAT transient monitor results provided by the Swift/BAT team, and the 15 GHz data provided by the OVRO team.

## REFERENCES

- Abdo, A. A., Abeysekara, A. U., Allen, B. T., et al. 2014, *ApJ*, **7824**, 110
- Abdo, A. A., Ackermann, M., Ajello, M., et al. 2011, *ApJ*, **736**, 131
- Abramowski, A., Acero, F., Aharonian, F., et al. 2012, *ApJ*, **746**, 151
- Acciari, V. A., Aliu, E., Arlen, T., et al. 2009a, *Sci*, **325**, 444
- Acciari, V. A., Aliu, E., Arlen, T., et al. 2011, *ApJ*, **738**, 25
- Acciari, V. A., Aliu, E., Aune, T., et al. 2009b, *ApJ*, **703**, 169
- Acciari, V. A., Arlen, T., Aune, T., et al. 2014, *Aph*, **54**, 1
- Aharonian, F. A. 2000, *NewA*, **5**, 377
- Aielli, G., Assiro, R., Bacci, C., et al. 2006, *NIMPA*, **562**, 92
- Aielli, G., Bacci, C., Bartoli, B., et al. 2010, *ApJL*, **714**, L208
- Ajello, M., Rau, A., Greiner, J., et al. 2008, *ApJ*, **673**, 96
- Albert, J., Aliu, E., Anderhubet, H., et al. 2007, *ApJ*, **663**, 125
- Aleksic, J., Ansoldi, S., Antonelli, L. A., et al. 2015a, *A&A*, **576**, 126
- Aleksic, J., Ansoldi, S., Antonelli, L. A., et al. 2015b, *A&A*, **578**, 22
- Amenomori, M., Ayabe, S., Chen, D., et al. 2005, *ApJ*, **633**, 1005
- Ammando, F. D., & Orienti, M. 2012, *ATel*, **#4261**
- Atwood, W. B., Abdo, A. A., Ackermann, M., et al. 2009, *ApJ*, **697**, 1071
- Bartoli, B., Bernardini, P., Bi, X. J., et al. 2011a, *ApJ*, **734**, 110
- Bartoli, B., Bernardini, P., Bi, X. J., et al. 2012a, *ApJL*, **745**, L22
- Bartoli, B., Bernardini, P., Bi, X. J., et al. 2012b, *ApJ*, **758**, 2
- Bartoli, B., Bernardini, P., Bi, X. J., et al. 2012c, *ApJ*, **760**, 110
- Bartoli, B., Bernardini, P., Bi, X. J., et al. 2012d, *PhRvD*, **85**, 022002
- Bartoli, B., Bernardini, P., Bi, X. J., et al. 2012e, *PhRvD*, **85**, 092005
- Bartoli, B., Bernardini, P., Bi, X. J., et al. 2012f, *ATel*, **#4272**
- Bartoli, B., Bernardini, P., Bi, X. J., et al. 2013a, *ApJ*, **779**, 27
- Bartoli, B., Bernardini, P., Bi, X. J., et al. 2013b, *ApJ*, **767**, 99
- Bartoli, B., Bernardini, P., Bi, X. J., et al. 2013c, *PhRvD*, **88**, 082001
- Bartoli, B., Bernardini, P., Bi, X. J., et al. 2014, *ApJ*, **790**, 152
- Bartoli, B., Bernardini, P., Bi, X. J., et al. 2015, *ApJ*, **798**, 119
- Blazewski, M., Blaylock, G., Bond, I. H., et al. 2005, *ApJ*, **630**, 130
- Burrows, D. N., Hill, J. E., Nousek, J. A., et al. 2005, *SSRv*, **120**, 165
- Cardelli, J. A., Clayton, G. C., & Mathis, J. S. 1989, *ApJ*, **345**, 245
- Cao, G., & Wang, J. C. 2013, *PASJ*, **65**, 109
- Chen, L. 2014, *ApJ*, **788**, 179
- Chen, S. Z. 2013, *SCPMA*, **56**, 1454
- Cheung, C. C., Harris, D. E., & Stawarz, L. 2007, *ApJL*, **663**, L65
- Dermer, C. D., Schlickeiser, R., Mastichiadis, A., et al. 1992, *A&A*, **256**, L27
- Drury, L. O. 1983, *RPPh*, **46**, 973
- Edelson, R. R., & Krolik, J. H. 1988, *ApJ*, **333**, 646
- Edelson, R. A., Alexander, T., Crenshaw, D. M., et al. 1996, *ApJ*, **470**, 364
- Fleysher, R., Fleysher, L., Nemethy, P., & Mincer, A. I. 2004, *ApJ*, **603**, 355
- Fortson, L., VERITAS Collaboration, Fermi-LAT Collaboration 2012, in AIP Conference Proceedings, Vol. 1505, 5th International Meeting on High Energy Gamma-Ray Astronomy, ed. F. A. Aharonian, et al. (New York: AIP), **514**
- Franceschini, A., Rodighiero, G., Vaccari, M., et al. 2008, *A&A*, **487**, 837
- Galante, N. for the VERITAS Collaboration 2011, in Proc. 32nd ICRC, Vol. 8 (Beijing: ICRC), 63
- Gehrels, N., Chincarini, G., Giommi, P., et al. 2004, *ApJ*, **611**, 1005
- Ghisellini, G., Celotti, A., Fossati, G., Maraschi, L., & Comastri, A. 1998, *MNRAS*, **301**, 451
- Guo, F., Li, H., Daughton, W., & Liu, Y. H. 2014, *PhRvL*, **113**, 155005
- Guo, Y. Q., Zhang, X. Y., Zhang, J. L., et al. 2010, *ChPhC*, **34**, 555
- Hovatta, T., Petropoulou, M., Richards, J. L., et al. 2015, *MNRAS*, **448**, 3121
- Isobe, N., Sugimori, K., Kawai, N., et al. 2010, *PASJ*, **62**, L55
- Kalberla, P. M. W., Burton, W. B., Hartmann, Dap., et al. 2005, *A&A*, **440**, 775
- Kino, M., Takahara, F., & Kusunose, M. 2002, *ApJ*, **564**, 97
- Kirk, J. G., & Duffy, P. 1999, *JPhG*, **25**, 163
- Krawczynski, H. 2004, *NewA Rev.*, **48**, 367
- Krimm, H. A., Holland, S. T., Corbet, R. H. D., et al. 2013, *ApJS*, **209**, 14
- Levine, A. M., Bradt, H., Cui, W., et al. 1996, *ApJL*, **469**, L33
- Massaro, F., Tramacere, A., Cavaliere, A., Perri, M., & Giommi, P. 2008, *A&A*, **478**, 395
- Matsuoka, M., Kawasaki, K., Ueno, S., et al. 2009, *PASJ*, **61**, 999
- Max-Moerbeck, W., Hovatta, T., Richards, J. L., et al. 2014, *MNRAS*, **445**, 428
- Meyer, E. T., Fossati, G., Georganopoulos, M., & Lister, M. L. 2012, *ApJL*, **752**, L4
- Nolan, P. L., Abdo, A. A., Ackermann, M., et al. 2012, *ApJS*, **199**, 31
- Ong, R. A. 2010, *ATel*, **#2443**
- Peng, Y. P., Yan, D. H., & Zhang, L. 2014, *MNRAS*, **442**, 2357
- Poole, T. S., Breeveld, A. A., Page, M. J., et al. 2008, *MNRAS*, **383**, 627
- Richards, J. L., Max-Moerbeck, W., Pavlidou, V., et al. 2011, *ApJS*, **194**, 29
- Roming, P. W. A., Kennedy, T. E., Mason, K. O., et al. 2005, *SSRv*, **120**, 95
- Schlaflly, E. F., & Finkbeiner, D. P. 2011, *ApJ*, **737**, 103
- Sikora, M., Begelman, M. C., & Rees, M. J. 1994, *ApJ*, **421**, 153
- Singh, K. K., Yadav, K. K., Chandra, P., et al. 2015, *Aph*, **61**, 32
- Shukla, A., Chitnis, V. R., Vishwanath, P. R., et al. 2012, *A&A*, **541**, 140
- Stecker, F. W., Baring, M. G., & Summerlin, E. J. 2007, *ApJL*, **667**, L29
- Ulucykont, M., Bernardini, E., Satalecka, K., et al. 2010, *A&A*, **524**, 48
- Ulucykont, M. & H.E.S.S. Collaboration 2011, arXiv:1106.1035
- Tueller, J., Baumgartner, W. H., Markwardt, C. B., et al. 2010, *ApJS*, **186**, 378
- Virtanen, J. J. P., & Vainio, R. 2005, *ApJ*, **621**, 313
- Wagner, R. 2008, arXiv:0808.2483v1
- Yan, D. H., Zeng, H. D., & Zhang, L. 2014, *MNRAS*, **439**, 2933
- Yan, D. H., Zhang, L., Yuan, Q., et al. 2013, *ApJ*, **765**, 122
- Zhang, J., Liang, E. W., Zhang, S. N., & Bai, J. M. 2012, *ApJ*, **752**, 157